GRANDMA and HXMT Observations of GRB 221009A - the Standard-Luminosity Afterglow of a Hyper-Luminous Gamma-Ray Burst

D. A. Kann,[1,*] S. Agayeva,[2] V. Aivazyan,[3,4] S. Alishov,[2] C. M. Andrade,[5] S. Antier,[6] A. Baransky,[7] P. Bendjoya,[8] Z. Benkhaldoun,[9] S. Beradze,[3,4] D. Berezin,[10] M. Boër,[6] E. Broens,[11] S. Brunier,[8] M. Bulla,[12,13,14] O. Burkhonov,[15] E. Burns,[16] Y. Chen,[17] Y. P. Chen,[17] M. Conti,[18] M. W. Coughlin,[5] W. W. Cui,[17] F. Daigne,[19] B. Delaveau,[20] H. A. R. Devillepoix,[21] T. Dietrich,[22,23] D. Dornic,[24] F. Dubois,[25,26] J.-G. Ducoin,[19] E. Durand,[20] P.-A. Duverne,[27] H.-B. Eggenstein,[28] S. Ehgamberdiev,[15,29] A. Fouad,[30] M. Freeberg,[31] D. Froebrich,[32] M. Y. Ge,[17] S. Gervasoni,[6] V. Godunova,[10] P. Gokuldass,[33] E. Gurbanov,[2] D. W. Han,[17] E. Hasanov,[2] P. Hello,[34] T. Hussenot-Desenonges,[34] R. Inasaridze,[3,4] A. Iskandar,[35] N. Ismailov,[36] A. Janati,[9] T. Jegou du Laz,[34] S. M. Jia,[17] S. Karpov,[37] A. Kaeouach,[38] R. W. Kiendrebeogo,[6,39,5] A. Klotz,[40,41] R. Kneip,[42] N. Kochiashvili,[3] N. Kunert,[22] A. Lekic,[20] S. Leonini,[18] C. K. Li,[17] W. Li,[17] X. B. Li,[17] J. Y. Liao,[17] L. Logie,[25,26] F. J. Lu,[17] J. Mao,[43,44,45] D. Marchais,[46] R. Ménard,[47] D. Morris,[48] R. Natsvlishvili,[3] V. Nedora,[23] K. Noonan,[48] K. Noysena,[49] N. B. Orange,[50] P.T.H. Pang,[51,52] H. W. Peng,[53] C. Pellouin,[19] J. Peloton,[34] T. Pradier,[54] O. Pyshna,[7] Y. Rajabov,[15] S. Rau,[25,26] C. Rinner,[9] J.-P. Rivet,[8] F. D. Romanov,[55] P. Rosi,[18] V. A. Rupchandani,[56,57] M. Serrau,[58] A. Shokry,[30] A. Simon,[59,60] K. Smith,[48] O. Sokoliuk,[7,10] M. Soliman,[61] L. M. Song,[17] A. Takey,[30] Y. Tillayev,[15,29] L. M. Tinjaca Ramirez,[18] I. Tosta e Melo,[62] D. Turpin,[63] A. de Ugarte Postigo,[6] S. Vanaverbeke,[25,26] V. Vasylenko,[59,60] D. Vernet,[64] Z. Vidadi,[36] C. Wang,[65] J. Wang,[17] L. T. Wang,[35] X. F. Wang,[53,66] S. L. Xiong,[17,†] Y. P. Xu,[17] W. C. Xue,[17] X. Zeng,[67] S. N. Zhang,[17] H. S. Zhao,[17] and X. F. Zhao[17]

[1]*Hessian Research Cluster ELEMENTS, Giersch Science Center, Max-von-Laue-Straße 12, Goethe University Frankfurt, Campus Riedberg, 60438 Frankfurt am Main, Germany*

[2]*N. Tusi Shamakhy Astrophysical Observatory, Azerbaijan National Academy of Sciences, settl. Y. Mammadaliyev, AZ 5626, Shamakhy, Azerbaijan*

[3]*E. Kharadze Georgian National Astrophysical Observatory, Mt. Kanobili, Abastumani, 0301, Adigeni, Georgia*

[4]*Samtskhe-Javakheti State University, Rustaveli Str. 113, Akhaltsikhe, 0080, Georgia*

[5]*School of Physics and Astronomy, University of Minnesota, Minneapolis, Minnesota 55455, USA*

[6]*Artemis, Observatoire de la Côte d'Azur, Université Côte d'Azur, Boulevard de l'Observatoire, 06304 Nice, France*

[7]*Astronomical Observatory Taras Shevshenko, National University of Kyiv, Observatorna Str. 3, Kyiv, 04053, Ukraine*

[8]*Laboratoire J.-L. Lagrange, Université de Nice Sophia-Antipolis, CNRS, Observatoire de la Côte d'Azur, 06304 Nice, France*

[9]*Oukaimeden Observatory, High Energy Physics and Astrophysics Laboratory, FSSM, Cadi Ayyad University, Av. Prince My Abdellah, BP 2390 Marrakesh, Morocco*

[10]*Main Astronomical Observatory of National Academy of Sciences of Ukraine, 27 Acad. Zabolotnoho Str., Kyiv, 03143, Ukraine*

[11]*Vereniging Voor Sterrenkunde, Balen-Neetlaan 18A, 2400, Mol, Belgium*

[12]*Department of Physics and Earth Science, University of Ferrara, via Saragat 1, I-44122 Ferrara, Italy*

[13]*INFN, Sezione di Ferrara, via Saragat 1, I-44122 Ferrara, Italy*

[14]*INAF, Osservatorio Astronomico d'Abruzzo, via Mentore Maggini snc, I-64100 Teramo, Italy*

[15]*Ulugh Beg Astronomical Institute, Uzbekistan Academy of Sciences, Astronomy Str. 33, Tashkent 100052, Uzbekistan*

[16]*Department of Physics & Astronomy, Louisiana State University, Baton Rouge, LA 70803, USA*

[17]*Key Laboratory of Particle Astrophysics, Institute of High Energy Physics, Chinese Academy of Sciences, Beijing 100049, People's Republic of China*

[18]*Montarrenti Observatory, S. S. 73 Ponente, I-53018 Sovicille, Siena, Italy*

[19]*Sorbonne Université, CNRS, UMR 7095, Institut d'Astrophysique de Paris, 98 bis bd Arago, 75014 Paris, France*

[20]*Institut Polytechnique des Sciences Avancées IPSA, 63 bis Boulevard de Brandebourg, 94200 Ivry-sur-Seine, France*

[21]*Space Science & Technology Centre, School of Earth and Planetary Sciences, Curtin University, GPO Box U1987, Perth, Western Australia 6845, Australia*

[22]*Institute for Physics and Astronomy, University of Potsdam, Haus 28, Karl-Liebknecht-Str. 24/25, 14476 Potsdam, Germany*

[23]*Max Planck Institute for Gravitational Physics (Albert Einstein Institute), Am Mühlenberg 1, 14476 Potsdam, Germany*

[24]*CPPM, Aix Marseille Univ, CNRS/IN2P3, CPPM, Marseille, France*

[25]*AstroLAB IRIS, Provinciaal Domein "De Palingbeek", Verbrandemolenstraat 5, 8902 Zillebeke, Ieper, Belgium*

[26]*Vereniging Voor Sterrenkunde (VVS), Oostmeers 122 C, 8000 Brugge, Belgium*

[27]*Université Paris Cité, CNRS, Astroparticule et Cosmologie, F-75013 Paris, France*

[28]*Volkssternwarte Paderborn, Im Schlosspark 13, 33104 Paderborn, Germany*

[29]*National University of Uzbekistan, 4 University Str., Tashkent 100174, Uzbekistan*

[30] National Research Institute of Astronomy and Geophysics (NRIAG), 1 El-marsad St., 11421 Helwan, Cairo, Egypt
[31] KNC, AAVSO, Hidden Valley Observatory (HVO), Colfax, WI, USA; iTelescope, New Mexico Skies Observatory, Mayhill, NM, USA
[32] School of Physics and Astronomy, University of Kent, Canterbury CT2 7NH, UK
[33] Department of Aerospace, Physics, and Space Sciences, Florida Institute of Technology, Melbourne, Florida 32901, USA
[34] IJCLab, Univ Paris-Saclay, CNRS/IN2P3, Orsay, France
[35] Xinjiang Astronomical Observatory (XAO), Chinese Academy of Sciences, Urumqi, 830011, People's Republic of China
[36] N.Tusi Shamakhy Astrophysical Observatory Azerbaijan National Academy of Sciences, settl.Y. Mammadaliyev, AZ 5626, Shamakhy, Azerbaijan
[37] CEICO, Institute of Physics of the Czech Academy of Sciences, Na Slovance 1999/2, CZ-182 21, Praha, Czech Republic
[38] Oukaimeden Observatory, Cadi Ayyad University, High Atlas Observatory, Morocco
[39] Laboratoire de Physique et de Chimie de l'Environnement, Universit
'e Joseph KI-ZERBO, Ouagadougou, Burkina Faso
[40] IRAP, Université de Toulouse, CNRS, UPS, 14 Avenue Edouard Belin, F-31400 Toulouse, France
[41] Université Paul Sabatier Toulouse III, Université de Toulouse, 118 Route de Narbonne, 31400 Toulouse, France
[42] K26 / Contern Observatory (private obs.), 1, beim Schmilberbour, 5316 Contern, Luxembourg
[43] Yunnan Observatories, Chinese Academy of Sciences, 650011 Kunming, Yunnan Province, People's Republic of China
[44] Center for Astronomical Mega-Science, Chinese Academy of Sciences, 20A Datun Road, Chaoyang District, 100012 Beijing, People's Republic of China
[45] Key Laboratory for the Structure and Evolution of Celestial Objects, Chinese Academy of Sciences, 650011 Kunming, People's Republic of China
[46] Observatoire du 'Crous des Gats', 31550 Cintegabelle, France
[47] Club d'astronomie Mont-Tremblant, 545 Chemin Saint-Bernard, Mont-Tremblant, Québec, Canada J8E 1S8
[48] University of the Virgin Islands, United States Virgin Islands 00802, USA
[49] National Astronomical Research Institute of Thailand (Public Organization), 260, Moo 4, T. Donkaew, A. Mae Rim, Chiang Mai, 50180, Thailand
[50] OrangeWave Innovative Science, LLC, Moncks Corner, SC 29461, USA
[51] Nikhef, Science Park 105, 1098 XG Amsterdam, The Netherlands
[52] Institute for Gravitational and Subatomic Physics (GRASP), Utrecht University, Princetonplein 1, 3584 CC Utrecht, The Netherlands
[53] Physics Department, Tsinghua University, Beijing, 100084, People's Republic of China
[54] Université de Strasbourg, CNRS, IPHC UMR 7178, 67000 Strasbourg, France
[55] AAVSO observer; Pobedy street, house 7, flat 60, Yuzhno-Morskoy, Nakhodka, Primorsky Krai 692954, Russia
[56] Brown University, Providence, RI 02912, Rhode Island, USA
[57] American University of Sharjah, Sharjah, UAE
[58] Société Astronomique de France, Observatoire de Dauban, FR 04150 Banon, France
[59] Astronomy and Space Physics Department, Taras Shevchenko National University of Kyiv, Glushkova Ave., 4, Kyiv, 03022, Ukraine
[60] National Center Junior Academy of Sciences of Ukraine, Dehtiarivska St. 38-44, Kyiv, 04119, Ukraine
[61] Department of Astronomy and Meteorology, Faculty of Science, Al-Azhar University, 11884 Nasr City, Cairo, Egypt
[62] INFN, Laboratori Nazionali del Sud, I-95125 Catania, Italy
[63] Université Paris-Saclay, Université Paris Cité, CEA, CNRS, AIM, 91191, Gif-sur-Yvette, France
[64] Observatoire de la Côte d'Azur, CNRS, UMS Galilée, France
[65] National Astronomical Observatories, Chinese Academy of Sciences, Beijing 100012, People's Republic of China
[66] Beijing Planetarium, Beijing Academy of Science and Technology, Beijing, 100044, People's Republic of China
[67] Center for Astronomy and Space Sciences, China Three Gorges University, Yichang 443000, People's Republic of China

ABSTRACT

GRB 221009A is the brightest Gamma-Ray Burst detected in more than 50 years of study. Here, we present observations in the X-ray and optical domains ranging from the prompt emission (optical coverage by all-sky cameras) up to 20 days after the GRB obtained by the GRANDMA Collaboration (which includes observations from more than 30 professional and amateur telescopes) and the *Insight*-HXMT Collaboration operating the X-ray telescope HXMT-LE. We study the optical afterglow both with empirical fitting procedures and numerical modeling. We find that the GRB afterglow, extinguished by a large dust column, is most likely behind a combination of a large Milky-Way dust column combined with moderate low-metallicity dust in the host galaxy. We find that numerical models describing the synchrotron radiation at the forward shock of a relativistic top-hat jet propagating through a constant density medium require extreme parameters to fit the observational data. Based on these observations, we constrain the isotropic afterglow energy $E_0 \sim 3.7 \times 10^{54}$ erg, the density of the ambient medium $n_{\rm ism} \gtrsim 1$ cm^{-3} and the opening angle of the jet core to be $\gtrsim 10.7°$. We do not find evidence (for or against) of jet structure, a potential jet break and the presence or absence of a SN. Placed in the global context of GRB optical afterglows, we find the afterglow of GRB 221009A is luminous but not extraordinarily so, highlighting that some aspects of this GRB do not deviate from the known sample despite its extreme energetics and the peculiar afterglow evolution.

Keywords: Gamma-ray bursts: Individual: GRB 221009A — Optical astronomy (1776) — Optical telescopes (1744) — Interstellar dust extinction (837)

1. INTRODUCTION

Gamma-ray bursts (GRBs) are among the most energetic phenomena detected in the Universe. They release extreme amounts of energy in soft γ-rays, up to $1M_\odot$ assuming isotropic emission (Kulkarni et al. 1999; Atteia et al. 2017), and can also be exceedingly luminous in the optical domain (Akerlof et al. 1999; Boër et al. 2006; Kann et al. 2007; Racusin et al. 2008; Bloom et al. 2009; Jin et al. 2023).

GRBs exhibit durations[1] from ms up to several hours (e.g., Thöne et al. 2011; Gendre et al. 2013; Levan et al. 2014a). They have been historically divided (Mazets et al. 1981; Kouveliotou et al. 1993) into two classes based on their duration and spectral hardness.

So-called "short/hard GRBs" have durations of a few seconds or less and a harder spectrum with respect to their isotropic energy release (e.g., Minaev & Pozanenko 2020; Agüí Fernández et al. 2021). They have been linked to gravitational waves (Abbott et al. 2017a,b,c; Goldstein et al. 2017), and their progenitors are supposed to be mainly coalescing compact objects such as binary neutron stars or neutron-star black-hole binary systems (for reviews, see Nakar 2007; Berger 2014). The general "short/hard" paradigm has been called into question especially with the long-duration event GRB 211211A (Rastinejad et al. 2022; Troja et al. 2022; Yang et al. 2022), which has been claimed to be associated with kilonova emission, a hallmark of compact binary mergers.

Conversely, so-called "long/soft GRBs" generally have durations greater than a few seconds, a softer spectrum, and their origin is most likely related to the core-collapse of rapidly rotating massive stars (Woosley 1993; Mösta et al. 2015). Similar to the case of short GRBs, the "long/soft" paradigm has been called into question by GRB 200826A, a sub-second GRB clearly associated with supernova (SN) emission (Ahumada et al. 2021; Zhang et al. 2021; Rossi et al. 2022). For reviews of long GRBs and their connection to stripped-envelope supernova explosions, see Gehrels et al. (2009); Hjorth & Bloom (2012); Cano et al. (2017).

The luminosity of GRB afterglows (in the X-ray to optical/Near-InfraRed [NIR] energy range) is moderately correlated with the isotropic prompt-emission (mostly γ-ray) energy release $E_{\rm iso}$ (Gehrels et al. 2008; Nysewander et al. 2009; Kann et al. 2010, 2011), so very luminous GRBs usually have more luminous afterglows, and of course a low distance also implies a brighter afterglow that can be more easily followed-up. A combination of these two features therefore usually yields the richest data sets for any electromagnetic study. Two examples of such well-studied, nearby bright GRBs are GRBs 030329 and 130427A. GRB 030329 occurred at $z = 0.16867 \pm 0.00001$ (Thöne et al. 2007), and is to this day the GRB afterglow with the most optical/NIR observations. It yielded data for a wide range of studies on the prompt emission, afterglow evolution and polarization, and the associated SN 2003dh (Vanderspek et al. 2004; Lipkin et al. 2004; Greiner et al. 2003; Hjorth et al. 2003; Stanek et al. 2003; Matheson et al. 2003). The second being GRB 130427A, the first known nearby GRB ($z = 0.3399 \pm 0.0002$, Selsing et al. 2019) that exhibited an $E_{\rm iso}$ in the range of "cosmological" GRBs at $z \gtrsim 1$. There is also a rich observational data set for this event, stretching from trigger time to nearly 100 Ms (e.g. Maselli et al. 2014; Vestrand et al. 2014; Ackermann et al. 2014; Perley et al. 2014; Melandri et al. 2014; Levan et al. 2014b; van der Horst et al. 2014; De Pasquale et al. 2016).

In this paper, we report observations by the GRANDMA collaboration and its partners of the paragon of nearby, bright GRBs, GRB 221009A, by far the brightest GRB observed to date.

On 9 October 2022, at 14:10:17 UT, the Burst Alert Telescope (BAT, Barthelmy et al. 2005) onboard the *Neil Gehrels Swift Observatory* satellite (Gehrels et al. 2004, *Swift* hereafter) triggered and located a new, X-ray

* Corresponding author: ultralonggrbsn@gmail.com
† Corresponding author: xiongsl@ihep.ac.cn

[1] Usually measured as T_{90}, denoting the time span during which 90% of the emission, from 5% to 95%, are accumulated. T_{90} durations are detector-dependent and can include γ-ray tail emission in bright bursts.

bright transient denoted as *Swift* J1913.1+1946 (triggers 1126853 and 1126854, Dichiara et al. 2022a,b). *Swift* slewed immediately to the position and its narrow-field instruments, the X-ray telescope (XRT, Burrows et al. 2005) and the Ultra-Violet/Optical Telescope (UVOT, Roming et al. 2005) discovered a transient, which was very bright in X-rays (> 800 ct/s) and moderately bright in the optical (unfiltered finding chart, *white* = 16.63 ± 0.14 mag). The optical detection was somewhat remarkable as the transient lies in the Galactic plane and extinction along the line-of-sight is very high, $E_{(B-V)} = 1.32$ mag/$A_V = 4.1$ mag (Schlafly & Finkbeiner 2011, henceforth SF11). It was furthermore reported that the source was also detected over ten minutes earlier by the Gas-Slit Camera (GSC) of the *MAXI* X-ray detector onboard the International Space Station (ISS, Negoro et al. 2022; Kobayashi et al. 2022; Williams et al. 2023). Overall, this is in agreement with a new Galactic transient.

About 6.5 hours after the *Swift* trigger, it was reported by Kennea et al. (2022a) that this source may be a GRB, GRB 221009A, as both the Gamma-Ray Burst Monitor (GBM, Meegan et al. 2009) and the Large Area Telescope (LAT, Atwood et al. 2009) of the *Fermi* observatory (GLAST Facility Science Team et al. 1999) triggered on a GRB[2] localized to the same sky position at 13:16:59.99 UT, which we henceforth use as trigger time T_0. This event turned out to be extraordinarily bright (Veres et al. 2022), not just the brightest event ever detected by GBM, but the brightest *ever* detected.

The event begins with a moderately bright precursor, followed by ≈ 180 s of quiescence before the main phase starts. The first peak, ≈ 20 s long, would already place GRB 221009A among the brightest GRBs ever detected, exceeding all but a handful of GBM/Konus detections. This peak is followed by two ultra-bright peaks, and finally a fourth, less bright but longer peak which fades into a high-energy afterglow at ≈ 600 s. The extreme fluence led to a saturation of all sensitive γ-ray detectors, such as *Fermi* GBM (Lesage et al. 2022), *Fermi* LAT (Bissaldi et al. 2022; Pillera et al. 2022; Omodei et al. 2022a,b), Konus-*Wind* (Frederiks et al. 2022), *Insight*-HXMT/HE (Tan et al. 2022; Ge et al. 2022), *AGILE*/MCAL+AC (Ursi et al. 2022), and *INTEGRAL* SPI/ACS (Gotz et al. 2022).

This saturation leads to preliminary analyses reporting only lower limits on the true fluence. *INTEGRAL* SPI/ACS (Gotz et al. 2022) analysis finds 1.3×10^{-2} erg/cm^2, *Fermi* GBM finds $(2.912 \pm 0.001)\times10^{-2}$ erg/cm^2 and peak flux 2385 ± 3 ph s^{-1} cm^{-2}, Konus-*Wind* report 5.2×10^{-2} erg/cm^2 (Frederiks et al. 2022), and Kann & Agui Fernandez (2022) estimate $\approx 9\times10^{-2}$ erg/cm^2. Even these preliminary estimates show GRB 221009A exceeded GRB 130427A in fluence by a factor of at least 10.

Several smaller orbital detectors were not saturated, stemming from size, environment, or off-axis detection, such as detectors on *Insight* (the Low-Energy (LE) telescope and the Particle Monitors, Ge et al. 2022), *SATech-01/GECAM-C* HEBS (Liu et al. 2022), *GRB-Alpha* (Ripa et al. 2022), *STPSat-6*/SIRI-2 (Mitchell et al. 2022), and *SRG*/ART-XC (Lapshov et al. 2022).

Optical spectroscopy of the transient showed it to indeed be a GRB afterglow, with a redshift $z = 0.151$ measured both in absorption and emission (de Ugarte Postigo et al. 2022; Castro-Tirado et al. 2022; Izzo et al. 2022, Malesani et al., in prep.), making it even closer than GRB 030329. Such an event is ultra-rare, e.g., Atteia (2022) estimate it to occur only once every half-millenium (see also Williams et al. 2023, Burns et al., in prep.).

The GRB showed very strong VHE emission, with a ≈ 400 GeV photon detected by *Fermi* LAT (Xia et al. 2022a,b), a highly significant detection by *AGILE*/GRID (Piano et al. 2022), photons of ≈ 10 GeV seen more than two weeks after the GRB by DAMPE (Duan et al. 2022), the spectacular detection by LHAASO of thousands of VHE photons up to 18 TeV (Huang et al. 2022), and potentially even a 250 TeV photon detected by Carpet-2 (Dzhappuev et al. 2022).

The burst caused a Sudden Ionospheric Disturbance (Schnoor et al. 2022; Guha & Nicholson 2022; Hayes & Gallagher 2022; Pal et al. 2023). There were no detected neutrinos associated with GRB 221009A, however (IceCube Collaboration 2022; KM3NeT Collaboration 2022; Ai & Gao 2022). The gravitational-wave detectors were off or not sensitive enough to achieve any detection (Pannarale 2022).

GRANDMA (Global Rapid Advanced Network for Multi-messenger Addicts) (Antier et al. 2020a,b; Aivazyan et al. 2022) is a collaboration of ground-based facilities dedicated to time-domain astronomy, and focused on electromagnetic follow-up of gravitational-wave candidates and other transients such as GRBs. Its network contains 36 telescopes from 30 observatories, 42 institutions, and groups from 18 countries[3]. The net-

[2] The initial GBM trigger notice was distributed, but a problem with automated data processing prevented any additional real-time classification/localization messages from being sent to the ground.

[3] https://grandma.ijclab.in2p3.fr

work has access to wide field-of-view telescopes ([FoV] > 1deg^2) located on three continents, and remote and robotic telescopes with narrower fields-of-view.

Here we present the analysis of the afterglow emission of GRB 221009A with different model approaches. All results are obtained using the *Fermi* GBM trigger time of 9 October 13:16:59.99 UT. In §2, we present the observational data we use in the article, the photometric methods we use and a discussion of the extinction selection. In §3, we present our methods to analyze the afterglow light curves using empirical light-curve fitting and two Bayesian inference analyses. We then present our results to investigate which astrophysical scenarios and processes best describe the data. In §4, we present our conclusions.

2. OBSERVATIONAL DATA

2.1. *Swift XRT and HXMT/LE afterglow data*

The *Swift* XRT started to observe the field of GRB 221009A right after BAT triggered on the afterglow, about 56 min after the *Fermi*/GBM trigger time. The X-ray light curve (0.3 – 10 keV) of GRB 221009A was collected from the UK *Swift* Science Data Centre[4] at the University of Leicester (Evans et al. 2007, 2009). We directly made use of the Burst Analyser light curves given in Jansky units at several central frequencies. Due to the large number of data points in the *Swift* XRT light curve, we could not use it directly for the MCMC analysis without overweighting the X-ray data. We therefore constructed a synthetic light curve of the *Swift* XRT data (both at 1 keV and 10 keV). We separated the observations into 16 time windows, fitting a Gaussian to the flux distribution of the observations in each time window. Its median value and standard deviation are used as the measure and error of the synthetic curve. The obtained synthetic light curve is presented in Fig. 1.

The *Insight*-HXMT/LE X-ray telescope (Zhang et al. 2020) detected the afterglow emission of GRB 221009A at late times from about 9.8 h to 3 d after the *Fermi*/GBM trigger time, including two scanning observations (P050124003601 & P050124003701) and 20 pointing observations ranging from P051435500101 to P051435500401 with a total good-time-interval of 24 ks. The first two points are obtained by the spectral fitting of two scanning observations. The spectrum is obtained from the data when the target appears in the FoV. Unlike the pointing observations, the background is not obtained by the background model but from a region with no bright source in the FoV. Moreover, the instrumental response is calculated with the target track in the FoV and the Point Spread Function (PSF) of the *Insight*-HXMT/LE collimator. For the pointing observations, we use the *Insight*-HXMT Data Analysis software HXMTDAS v2.05[5] to extract the light curves, spectra and background following the recommended procedure of the *Insight*-HXMT Data Reduction for HXMT-LE analysis. For both the scanning and pointing observations, the spectra of *Insight*-HXMT/LE in the 1.5 – 10 keV range are fitted by an absorbed power-law, i.e., tbabs*power in XSPEC. The HXMT/LE X-ray afterglow is shown in comparison to the *Swift*/XRT measurements in Fig. 1.

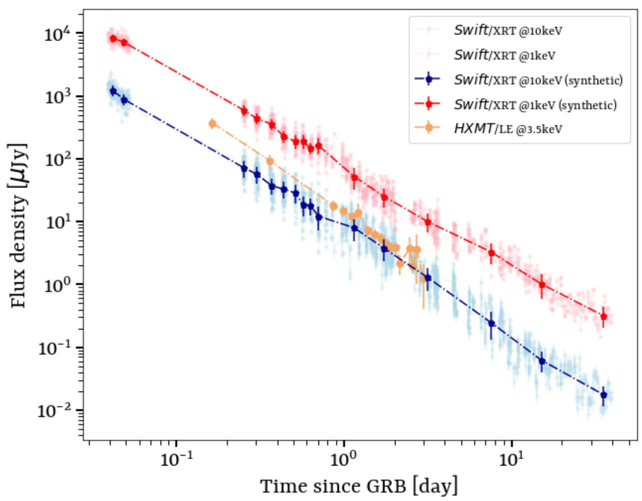

Figure 1. The unabsorbed X-ray light curve of GRB 221009A detected by the *Swift*/XRT (given at 10 keV in blue and 1 keV in red) and the HXMT/LE (orange) instruments. The light curves were corrected for Galactic and intrinsic NH I column density absorption estimated from the late-time *Swift*/XRT spectrum analysis (https://www.swift.ac.uk/xrt_spectra/01126853/). In dark blue and red colors, we show our synthetic *Swift*/XRT light curve that we finally used in our afterglow modeling analysis, see the sections 3.4.2 and 3.4.1.

2.2. *Optical observations during the GRB prompt emission*

We used the images taken from two sites managed by the Desert Fireball Network (Towner et al. 2020) at Mundrabilla (lon = 127.8486° E, lat = 31.8356° S, altitude = 84 m) and at Raw War Road (lon = 125.7503° E, lat = 29.7422° S, altitude = 215 m), Western Australia. The acquisition devices are constituted of a

[4] https://www.swift.ac.uk/

[5] http://hxmtweb.ihep.ac.cn/

Nikon D810 (color CFA matrix) set at 3200 ISO with Samyang 8mm F/3.5 optics. This provides images covering the full sky. Images have 27 s exposure time taken every 30 seconds for the entire night. At the prompt time the GRB is located at elevations of 15° and 17° above the local horizons of Mundrabilla and Raw War Road, respectively. The sky at Mundrabilla was partially covered by thin clouds and there was bright moonlight. Weather and elevation conditions were better at Raw War Road. We analyzed the archive images taken between $t_{GRB}-30$ s and $t_{GRB}+500$ s. There is no detection at the position of the GRB to a limiting magnitude of 3.8 mag in the Green filter (which is roughly compatible with Johnson V) at Raw War Road. The limits are shallower at Mundrabilla. Time and magnitudes in the AB system are reported in Table 3 corrected for extinction and in the Appendix, Table 4 uncorrected for extinction. No other contemporaneous observations have been reported, so to our knowledge, these are unique.

2.3. *Optical post-GRB observations*

Our first observation of the GRB within GRANDMA was obtained with the TAROT-Réunion telescope (TRE) at 2022-10-09T15:34:41 UTC (2:20 hr after T_0) thanks to its automated program following GRBs. Although GRANDMA was not conducting an observational campaign at the time of event, by the request of A. de Ugarte Postigo, the GRANDMA network was activated to observe about 1 day post-trigger time; at this point, we provided the network the *Swift* UVOT coordinates (Dichiara et al. 2022b). The first ToO image requested by GRANDMA was taken by the 60 cm telescope from Maidanak $\sim$ 90 min after the notification at 2022-10-10T14-56-43 UTC (1.08 d after the GBM trigger) with the R_C filter. Our last observations were made by the Canada-France-Hawaii Telescope (CFHT) equipped with Megacam at 2022-10-29T06:32 (19 d, 17 hr post T_0). In total, we collected about 80 images (usually consisting of stacks of short exposures) from 15 GRANDMA partner telescopes. In successive order, we provide here the mid-time of the first observation relative to T_0 for each telescope and the filters used during the whole campaign: D810 (before and during the prompt emission in V band) at Mundrabilla and Raw War Road observatories, TAROT-Réunion (0.0972 d, without filter) near Les Makes Observatory, UBAI-ST60 (1.0813 d in R_C) at Maidanak Observatory, KAO (1.1368 d in $g'r'i'z'$) at Kottamia Observatory, ShAO-T60 (1.1465 d in VR_C) at Shamakhy Observatory, AZT-8 (1.2274 d in R_CI_C) at Lisnyky observatory, HAO (1.2563 d without filter) at Oukaimenden observatory, MOSS (1.2722 d without filter) at Oukaimenden Observatory, C2PU-Omicron (1.3077 d in r') at Calern observatory, SNOVA (2.1535 d without filter) at Nanshan Observatory, T70 (2.2424 d in I_C) at Abastumani Observatory, UBAI-AZT22 (11.1313 d in R_C) at Maidanak Observatory, VIRT (12.4567 d in R_CI_C) at Etelman Observatory, and CFHT-Megacam (19.6945 d in $g'r'i'z'$) at Mauna Kea Observatory. Our preliminary analysis of the GRANDMA observations has been reported by Rajabov et al. (2022) where we reported observations from UBAI-ST60, KAO, Lisnyky-AZT-8, MOSS, C2PU-Omicron and SNOVA. In general, the sensitivity of the observations at the earliest epochs was reduced by the full moon.

In addition to the professional network, GRANDMA activated its Kilonova-Catcher (KNC) citizen science program for further observations. Our web portal was used to provide coordinates of the *Swift* UVOT source. Some amateur astronomers participating in the program observed the source by their own volition and distributed their own reports to the astronomical community (Broens 2022; Romanov 2022a,b,c; Aguerre et al. 2022). They also transferred their images to our web portal to allow us to perform our own image reduction and analysis. In total more than 250 images were uploaded to our web portal. Here we provide the list of contributors and the respective names for the telescopes (and their identifiers in Tables 3 and 4 when the images were selected for a photometric analysis) : M. Freeberg / a Celestron C11-Edge telescope, the iT11 and iT21 iTelescopes (KNC-C11-FREE, KNC-iT11 and KNC-iT21); S. Vanaverbeke / the NMPT Astrolab IRIS 0.68m telescope (KNC-IRIS); R. Menard / the Celestron EdgeHD14 (KNC-C14/Ste-Sophie); M. Richmond / the 12" MEADE telescope at the RIT Observatory; M. Serrau / the C11 Dauban MSXD Telescope (KNC-MSXD); S. Leonini / the 0.53-m Ritchey-Chretien telescope of Montarrenti Observatory (KNC-Montarrenti); H. B. Eggenstein / the OMEGON200F5Newton telescope (KNC-EHEA-200F5); G. Parent / a Newton SW 200/1000 telescope (KNC-Parent); O. Aguerre / a Newton 250 f/4 telescope, E. Maris / a Celestron 11 ATLAS telescope (KNC-C11-ATLAS); D. Marchais / the T-CAT telescope at the Crous des Gats Observatory (KNC-T-CAT); F. D. Romanov / the iT24 iTelelescope of the Sierra Remote Observatory and the 0.61-m Dall-Kirkham telescope of Burke-Gaffney Observatory (KNC-iT24 and KNC-BGO); E. Broens / the 0.28m Mol SCT (KNC-SCT-0.28); A. Lekic / the LCO 0.4m telescope at the McDonald Observatory (KNC-LCO/McDO-0.4m); F. Bayard / a Celestron C11 Millery telescope; and R. Kneip / the Planewave CDK-14 telescope at the Contern Observatory K26 (KNC-COK26).

The observations started 0.25 to ~ 6 days after the trigger time, predominantly in Johnson-Cousins and Sloan filter sets, but also with other filters, such as *Lumen* or Bayer sensors.

The GRANDMA observations are listed in Tables 3 and 4. The former reports the mid-time (in ISO format with post-trigger delay) and extinction-corrected brightness (in AB magnitudes) of the observations, while the latter includes the uncorrected magnitudes and references to selected online GCN reports (see public observational reports, individual GCNs are all cited in the table). The mid-time is calculated as the weighted average of the observation start time and the number of exposures. The number of exposures is also provided. Our method for calculating magnitudes is described in the following section, and images that did not meet our criteria are labeled as "VETO". In Table 4, the reference catalogs and stars used by external teams for comparison are also included, unless not specified in the GCN reports. When the information is not provided by the online GCN report, we mark it as "-".

2.4. *Photometric methods*

We requird all GRANDMA images to be pre-processed by the telescope teams with bias or dark subtraction and flat-fielding. We reject a few images from amateur astronomers where these corrections were not performed. Some teams uploaded their images with their own astrometric calibration, but for most images the astrometric calibration is obtained directly from the Astrometry.net website. Then, two methods are used to measure the magnitude on the template-subtracted images (see below): **STDpipe** and **MUPHOTEN**. For both of these methods, we use techniques to blindly search for new detections within the *Swift* UVOT error localization (Dichiara et al. 2022b), but we can also force photometry at the GRB 221009A afterglow coordinates we fixed to RA = 288.2646558, Dec. = 19.7733650 (Atri et al. 2022).

STDpipe – The Simple Transient Detection Pipeline STDPipe (Karpov 2021), is a set of python libraries aimed at performing astrometry, photometry and transient detection tasks on optical images. To do so, it uses several external algorithms such as SExtractor (Bertin & Arnouts 1996) for the source extraction, catalog cross-matching tools using the CDS Xmatch service developed at the Strasbourg Astronomical Observatory (Boch et al. 2012; Pineau et al. 2020), the hotpants code (Becker 2015) for image subtraction tasks and the photutils[6] Astropy package (Bradley et al. 2021) to perform photometric calibration and measurements. More details about the STDPipe software architecture can be found in the git documentation[7]. In order to increase the signal-to-noise ratio of some KNC images where the GRB afterglow was barely visible, we resampled and coadded individual frames using the Swarp software (Bertin 2010). Our final set of science images were subtracted with Pan-STARRS DR1 catalog (PS1, Chambers et al. 2016) images downloaded from the CDS HiPS2FITS service (Boch et al. 2020) and rescaled to each image pixel scale. Forced aperture photometry was then applied at the GRB afterglow position. Due to the heterogeneity of the KNC instruments, we had a wide pixel scale distribution in our images. Therefore, the aperture radius was fixed per image to the average FWHM of stars detected at S/N > 5 by SExtractor in the image field. Depending on the photometric system used by KNC astronomers, the photometric calibration was done with the stars in the image field either using the native photometric bands ($g'r'i'z'$) of the PS1 catalog or by converting them into the Johnson-Cousins BVR_CI_C system using the transformation described by Pancino et al. (2022). Finally we added a color correction term to the estimation of the zero point magnitude in order to take into account the color distribution of the PS1 calibration stars. Our KNC photometric results are shown in Table 3 and 4.

MUPHOTEN – Muphoten[8] is a Python-based software dedicated to photometry of transients observed by heterogeneous instruments, developed for the analysis of GRANDMA images (Duverne et al. 2022). Similarly to STDPipe, it uses Python libraries like photutils (Bradley et al. 2021) and external algorithms like SExtractor (Bertin & Arnouts 1996) and hotpants (Becker 2015). The Muphoten software was utilized for the analysis of all GRANDMA images and a portion of KNC images. We first construct a template image by mosaicking Pan-STARRS DR1 (PS1) archive images, matching the image FoV, and we use hotpants to subtract the template from the image. However, for a limited number of images, the template subtraction was unsuccessful due to non-convergence with hotpants. Nevertheless, these images had adequate resolution to clearly distinguish the transient from neighboring sources, so they were retained for further analysis. The background is estimated using the same method de-

[6] https://github.com/astropy/photutils

[7] https://github.com/karpov-sv/stdpipe

[8] https://gitlab.in2p3.fr/icare/MUPHOTEN

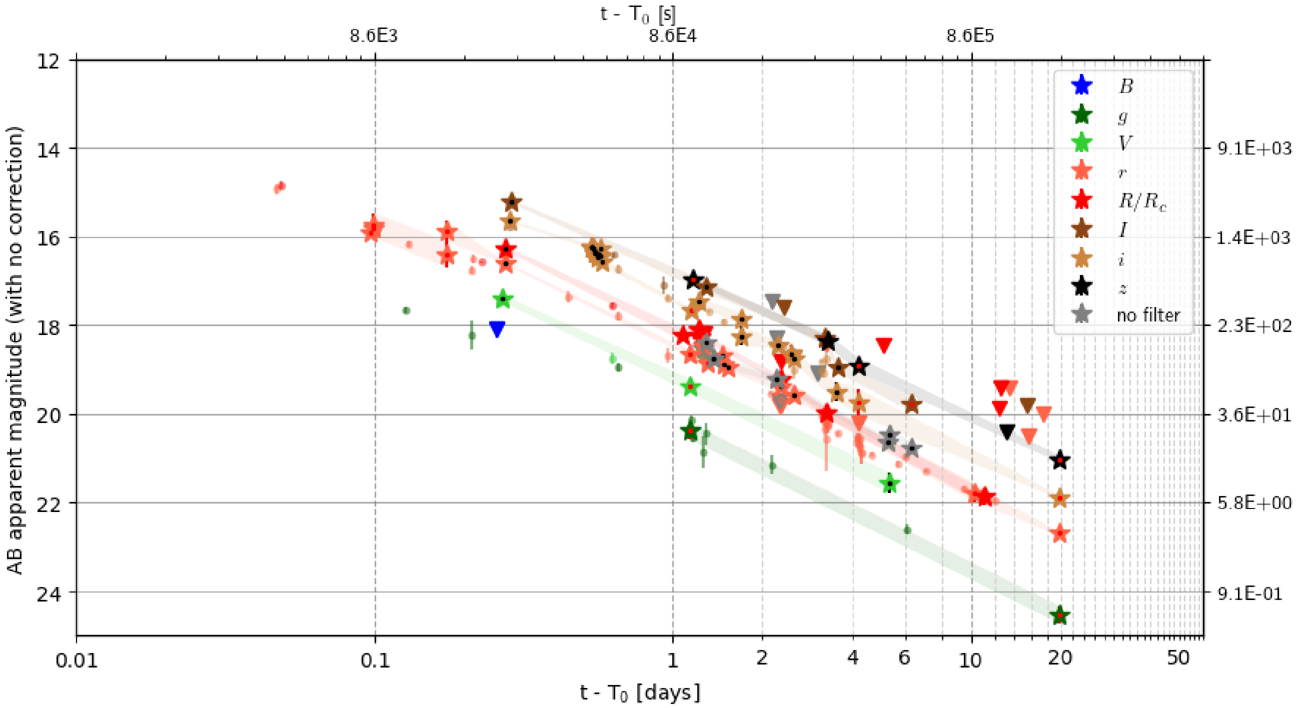

Figure 2. The optical afterglow of GRB 221009A was observed using $g'Vr'R_Ci'I_Cz'$ filters and without filter, with data points shown in the observer frame. The selected optical GCN data we use are represented by dots and the GRANDMA data measurements and upper limits are indicated by larger stars and downward-pointing triangles (see Table 4). The red points within the stars indicate measurements made by professional observers, while black points represent observations made by KNC observers. Only magnitude measurements with at least a 3σ detection significance are included (the upper limits being given at 5σ significance), with uncertainty regions shown as shading. The measurements are not corrected for any extinction.

scribed (SExtractor), in a mesh of 150×150 pixels by default (smaller grids were applied for images with rapidly varying backgrounds). The background and its standard deviation are interpolated to each pixel of the image and subtracted to obtain the final result. Sources are detected by identifying clusters of at least five neighboring pixels that exceed a threshold of 2σ above the background.

Next, we conducted isophotal photometry on all detected sources. The sources were cross-matched with the PS1 catalog, yielding the PS1 magnitudes of the matched sources in the corresponding filter. For images taken with Johnson-Cousins filters, we transformed the PS1 magnitudes to the observed filters using the conversion equations from Kostov & Bonev (2018). Unfiltered images were treated as if they were taken with the Cousins R_C filter and were processed using the same conversion equations. We construct a calibration scale by fitting the instrumental magnitude and PS1 magnitude using a first-order polynomial fit with iterative clipping of outliers (3σ away from the fit). We then compute calibrated magnitudes for all detected sources, sort them by distance to expected transient coordinates, and consider a source a detection if its coordinates match within five pixels. Due to crowding in the Galactic plane, we checked for neighboring objects affecting the automatically computed apertures, reducing them if necessary. Forced photometry using circular apertures of default radius 1.5 times the average FWHM of stars in the image was performed at the GRB coordinates in the absence of direct detection. This was calculated using the PSFEx software (Bertin 2011). Plotting circular apertures of increasing radius (1 to 10 pixels) and their corresponding measured fluxes, we could check whether the default aperture collected all the transient flux and not neighbouring sources, and manually correct its coordinates and radius when needed.

Finally, Muphoten assesses the sensitivity of the image with upper-limit estimations. In Muphoten, upper limits are computed as global properties of the whole studied image. The default method outlined in Duverne et al. (2022) calculates the success rate of recovering PS1 objects based on 0.2 magnitude intervals and selects the faintest interval where more than 10% of PS1 objects in the field-of-view are detected in the image. In the case of images where there is a high detection rate up until the limit of the Pan-STARRS catalog, an alternative method defines the upper limit as the magnitude of the faintest source detected with a SNR > 5.

2.5. *Extinction selection*

Unfortunately for optical studies, the brightest GRB ever detected lies behind significant extinction near the Galactic plane ($b = 4.32°$). Following the maps of SF11, the line-of-sight at the "reference pixel" lies behind $E_{(B-V)} = 1.32$ mag/$A_V = 4.1$ mag. However, at Galactic latitudes $|b| < 5°$, the maps of Schlegel et al. (1998, which those of SF11 are based on) are known to be unreliable and may overestimate the extinction (Popowski et al. 2003, and references therein).

Rowles & Froebrich (2009, henceforth RF09) presented a method of determining extinction towards the Galactic plane using near-infrared color excess determinations based on 2MASS observations, following earlier work from Froebrich et al. (2005) based on stellar counts. Using their extinction calculator[9] and the position of the GRB, we find a significantly lower extinction, using the 100NN (Nearest Neighbour, see RF09 for details) result (which has the highest S/N), of $A_V = 2.195$ mag. Using the classical Milky Way extinction curve of Cardelli et al. (1989, henceforth CCM89), this translates into $E_{(B-V)} = 0.709$ mag. The extinction maps of RF09 show that extinction toward this region of the Milky Way is smooth and quite homogeneous for several degrees around (and not high in the context of the potential extinction toward the Milky Way), the nearest pronounced molecular clouds with significantly higher extinction lie closer to the plane in the neighboring constellation Vulpecula, about 5° away. Therefore, we deem the use of the extinction curve of CCM89 to be valid.

Is this extinction value more realistic than that of SF11? The method of RF09 extends only[10] to $2-3$ kpc. There is evidence for additional dust screens at larger distances, however. *Swift* XRT observations reveal expanding rings in the X-rays (Tiengo et al. 2022) arising from scattering on distant dust curtains. These authors report the discovery of nine dust rings and derive the distances, with the most distant one lying at 3635 ± 36 pc, potentially already beyond the detection range of the RF09 method. Observations with IXPE (Negro et al. 2023) confirm the most distant dust ring found by *Swift* at 3.75 ± 0.0375 kpc, and report an even more distant dust curtain at 14.41 ± 0.865 kpc. Recently, Vasilopoulos et al. (2023) reported a detailed analysis of *Swift* XRT data and also find evidence for dust out to 15 kpc (see Williams et al. 2023 for further analysis).

[9] https://astro.kent.ac.uk/~df/query_input.html

[10] Neckel & Klare (1980) give a value of $A_V = 3.3$ mag along this sightline out to 3 kpc.

The Galactic disc exhibits a warp (e.g., Hou & Han 2014, and references therein). The map derived by Hou & Han (2014, their Fig. 16) shows that at the Galactic longitude of GRB 221009A ($l = 52.96°$), HII regions indeed extend up to several hundred pc "above" the Galactic plane. For the Galactic latitude of GRB 221009A ($b = 4.32°$), the sightline lies ≈ 1100 pc above the plane at a distance of 14.4 kpc, beyond the HII regions mapped by Hou & Han (2014). However, this does not rule out the existence of cold dust curtains even that high above the Galactic disc which would contribute extra extinction beyond the RF09 measurement. We therefore conclude the true extinction value along the line of sight to GRB 221009A lies in the interval of $A_V = 2.2-4.1$ mag, and will discuss both extreme values.

3. MULTI-WAVELENGTH ANALYSIS OF THE AFTERGLOW

To analyze the afterglow light curve, we use data from multiple sources: Our own GRANDMA and KNC data (see Table 3), selected GCN data (see Table 4), as well as data published in Williams et al. (2023); Shrestha et al. (2023); Laskar et al. (2023). Near-infrared observations are taken from Durbak et al. (2022); D'Avanzo et al. (2022); Huber et al. (2022); Ferro et al. (2022); O'Connor et al. (2022c,d).

3.1. *Empirical Light-Curve Analysis*

With the exception of our shallow upper limits from Mundrabilla and Raw War Road, no optical observations have been reported before the *Swift* trigger.

The first observations, consisting of *Swift* UVOT data from Williams et al. (2023); Laskar et al. (2023) and obtained via automatic analysis[11] as well as some ground-based observations (Belkin et al. 2022c; Xu et al. 2022), are found to decay more steeply than following observations (see below), and also lie above the back-extrapolation of that data. This indicates an extra component in the light curve, potentially the tail end of a reverse-shock flash. The extreme intensity of the GRB makes it potentially possible that the early transient was extremely bright.

Fitting a joint multiband fit to the data, which assumes achromatic evolution and leaves only the normalization of each band an independent parameter, we derive a decay slope of $\alpha_{Flash} = 1.18 \pm 0.15$ ($\chi^2/d.o.f. = 0.83$, we define $F_\nu \propto t^{-\alpha}\nu^{-\beta}$), significantly steeper than the later decay, but quite shallow for a reverse-shock flash (Sari & Piran 1999; Kobayashi 2000). As the

[11] https://swift.gsfc.nasa.gov/uvot_tdrss/1126853/index.html

baseline is short, it is possible we are seeing the transition from the early, steeply decaying component to the later shallower light-curve decay, and the decay at even earlier times might have been steeper and more in accordance with a reverse-shock flash. Extrapolating this slope backward to the peak of the brightest gamma-ray flare of the prompt emission, at ≈ 220 s post-trigger, we find $R_{AB} \approx 11$ mag ($R_{AB} \approx 7.6$ mag when corrected for SF11 extinction). This value is far fainter than our Mundrabilla/Raw War Road exposures probe. A steeper decay (see above) or an additional component directly associated with the prompt emission cannot be ruled out but would still be unlikely to be bright enough to be detected by our shallow all-sky observations.

Data at > 0.09 d can be fit with a smoothly broken power-law, with parameters pre-break slope α_1, post-break slope α_2, break time t_b in days, and break smoothness n. The very last data points at $\gtrsim 30$ d show a flattening that may result from the host galaxy becoming dominant, we exclude these data points from the analysis. We see no direct evidence of a SN component in the late light curve[12], in agreement with Shrestha et al. (2023), similar to the case of GRB 030329 (e.g., Kann et al. 2006), and therefore also do not include such a component in the fit. A dedicated search will need well-calibrated late-time data. In general, the data shows dispersion, leading to a large χ^2.

This fit results in $\alpha_1 = 0.834 \pm 0.013$, $\alpha_2 = 1.451 \pm 0.003$, $t_b = 0.590 \pm 0.013$ d, and a sharp break $n = 100$ fixed, with $\chi^2/d.o.f. = 6.95$. This steepening had also been reported by D'Avanzo et al. (2022), who found $\alpha_1 \approx 0.8$, $\alpha_2 \approx 1.6$, and $t_b \approx 0.98$ d based on a significantly smaller data set. Shrestha et al. (2023) find $\alpha_1 = 0.64$, $\alpha_2 = 1.44$ in r' and $\alpha_1 = 0.81$, $\alpha_2 = 1.46$ in i', similar to our result. Williams et al. (2023), using only *Swift* UVOT data, find $\alpha_{1,O} = 0.98^{+0.05}_{-0.11}$, $\alpha_{2,O} = 1.31^{+0.07}_{-0.05}$, and $t_{break,O} = 0.255^{+0.197}_{-0.127}$ d, in agreement with our results within 2σ. They point out this decay is clearly slower than that of the X-rays (see below), but is very unlikely to be influenced by a host or SN component.

Swift XRT observations (initially reported in Kennea et al. 2022b; Tohuvavohu et al. 2022, but these reports are based on the *Swift* trigger time) as given in the XRT repository (Evans et al. 2007, 2009) show the light curve[13] to have multiple shallow breaks (see also Williams et al. 2023, who caution that especially during the WT mode observation, the dust-scattering rings can influence the light curve stemming from the atypical background around the afterglow PSF), but within the first ≈ 10 d, the decay slope is $\alpha_X \approx 1.5-1.6$, similar but steeper than our optical result. In their detailed analysis, Williams et al. (2023) find $\alpha_{1,X} = 1.498 \pm 0.004$, $\alpha_{2,X} = 1.672 \pm 0.008$, and $t_{break,X} = 0.914^{+0.127}_{-0.116}$ d. *Insight*-HXMT observations (Ge et al. 2022) also yielded a somewhat steeper slope $\alpha_X \approx 1.66$. NICER observations also find $\alpha_X \approx 1.6$ (Iwakiri et al. 2022). The significantly more shallow decay phase in the optical ($\alpha_O \approx 0.83$) as well as the earlier break at $t_b \approx 0.6$ d are not seen in X-rays at all. The optical light curve also shows a much stronger break with $\Delta\alpha_O = 0.617 \pm 0.013$ vs. $\Delta\alpha_X = 0.174 \pm 0.009$.

3.2. *Analysis of the Spectral Energy Distribution*

The normalizations derived from the joint multiband fit described in §3.1 yield a Spectral Energy Distribution, a very low-resolution "spectrum" of the afterglow that is nonetheless valuable to study the dust properties along the line-of-sight. The fit assumes achromaticity, i.e., no spectral evolution, and is therefore based on all data involved in the fit. Except for scaling, the SED is identical at any time point covered by the fit, the specific values are measured at break time.

We fit the SED both without extinction (a simple power-law) as well as with Milky Way (MW), Large (LMC) and Small Magellanic Cloud (SMC) dust following the parametrization by Pei (1992). These fits are performed after correction for Galactic extinction, and we study both the RF09 and SF11 models.

The derived SED shows scatter, with especially the z' band deviating and being too faint. The field is not covered by the Sloan Digital Sky Survey (e.g., Almeida et al. 2023, and references therein); however, many telescopes use filters which are close to the SDSS system. There are offsets to the Pan-STARRS system which was used for calibration in most cases. Following the Pan-STARRS to SDSS conversion of Tonry et al. (2012), we find $g'_{PS1} - g'_{SDSS} = -0.26$ mag, $r'_{PS1} - r'_{SDSS} = 0.02$ mag, $i'_{PS1} - i'_{SDSS} = 0.03$ mag, and $z'_{PS1} - z'_{SDSS} = 0.13$ mag, i.e., small changes for $r'i'$ but more significant changes to g' and z'. As we are unable to examine each measurement individually for more precise color terms, we just apply these offsets to the four data points in the

[12] Note that data presenting evidence of a photometric SN rise (Belkin et al. 2022a,b) were taken under inclement conditions and are likely the result of blending with nearby sources and are therefore too bright (A. Pozanenko, priv. comm.). However, Fulton et al. (2023) assume an intrinsic optical decay slope identical to the X-ray slope and interpret the more shallow decay as a rising, luminous SN component.

[13] https://www.swift.ac.uk/xrt_live_cat/01126853/

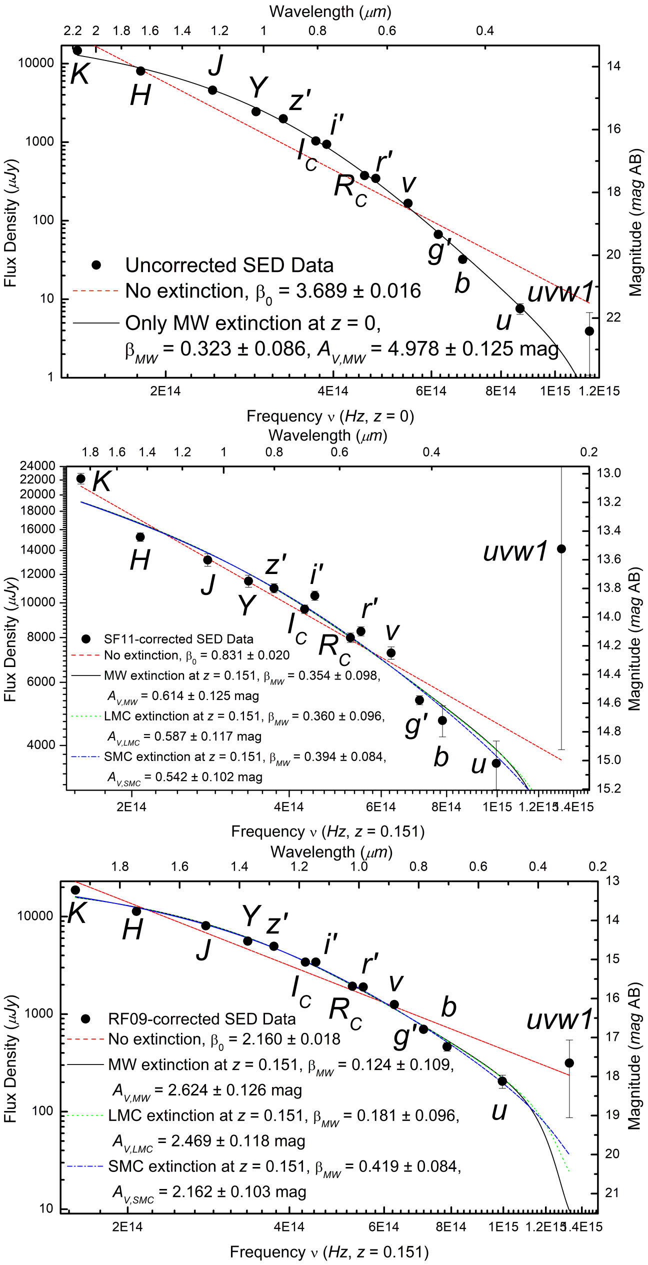

Figure 3. Analysis of the SED. **Top panel:** Fit to the uncorrected SED with a MW extinction model at $z = 0$, i.e., assuming no additional host-galaxy extinction. The fit is generally in agreement with the data, with the $uvw1$ data point being brighter than the model. **Middle panel:** Fit to the SED after correcting it for SF11 foreground extinction and shifting it to $z = 0.151$. The correction leads to significant scatter, with the $uvw1$ now being clearly brighter than any fit, even one without additional host-galaxy extinction. The three extinction laws can not be discerned from each other, but the potential bright $uvw1$ emission makes the SMC law the preferred one. **Bottom panel:** As the middle panel, with RF09 foreground extinction. The SED remains very red, and very high host extinction is implied. SMC extinction again leads to the most physical solution, but all dust laws are in conflict with the bluest *Swift* UVOT detection.

SED, which leads to a marked reduction in scatter and χ^2.

3.2.1. *Pure MW extinction*

We first study the SED without applying any MW foreground correction, and taking the data at $z = 0$. The SED is very steep and shows evidence for curvature (see Fig. 3, top panel). A simple power-law fit yields a spectral slope $\beta_0 = 3.689 \pm 0.016$. This is clearly not a good model, we find $\chi^2/d.o.f. = 160$ for twelve degrees of freedom.

Applying MW dust to the SED yields a highly significant improvement ($\chi^2/d.o.f. = 7.1$ for eleven degrees of freedom), and we derive $\beta = 0.323 \pm 0.086$, $A_{V,Gal} = 4.978 \pm 0.125$ mag ($E_{(B-V)} = 1.62 \pm 0.04$ mag). This value exceeds the SF11 correction by nearly a magnitude and can indicate two things: Either even the SF11 result does not encompass the entirety of the MW foreground extinction, or there is additional, significant host-galaxy extinction along the line of sight, or it is a combination of both at once. The detection of the Na I doublet at the redshift of the host galaxy (de Ugarte Postigo et al. 2022, Malesani et al., in prep.) indicates there must be some amount of host-galaxy extinction. However, we note that the free fit already yields an intrinsic spectral slope lying in the typical range found for GRB afterglows, $\beta \sim 0.2 - 1.2$ (Kann et al. 2010).

3.2.2. *SF11 extinction*

We next correct the SED for SF11 MW extinction and now study the pure host extinction at $z = 0.151$. After this correction, the spectral slope is obviously much flatter than before ($\beta_{0,SF11} = 0.831 \pm 0.020$, $\chi^2/d.o.f. = 7.7$ for ten degrees of freedom), however, the SED shows scatter (see Fig. 3, middle panel), with especially the $uvw1$ band deviating. We caution this color is derived versus only two r'/R_C-band GCN points, which can create additional insecurity. If real, the $uvw1$ band detection (Williams et al. 2023) coincides with the 2175 Å bump feature for LMC and MW dust in the host-galaxy rest frame, indicating the host-galaxy extinction law is most likely similar to SMC dust which lacks this feature almost completely. Mathematically, the different results can not be distinguished ($\chi^2/d.o.f. = 6.1$, 6.0, 5.7 for MW, LMC, and SMC dust, respectively; see also Williams et al. 2023), but SMC dust yields the overall most logical result, with an intrinsic spectral slope very close to the MW-only fit ($\beta_{SF11,SMC} = 0.394 \pm 0.084$) and moderate additional host-frame extinction ($A_{V,SF11,SMC} = 0.542 \pm 0.102$ mag). Using only *Swift* UVOT data, Williams et al. (2023) derive higher values: Correcting for the higher foreground extinction given by Schlegel et al. (1998) and using an intrinsic slope of

$\beta = 0.7$, they find $E_{(B-V)} = 0.51 \pm 0.03$ mag for SMC dust.

3.2.3. *RF09 extinction*

Finally, for the lowest assumed MW extinction, that of RF09, we find a combination of "moderately high" MW extinction and "moderately high" host-galaxy extinction. The SED after RF09 correction is still very steep (see Fig. 3, bottom panel, we find $\beta_{0,SF11} = 2.160 \pm 0.018$, $\chi^2/d.o.f. = 47$). Again the three dust models yield similar goodness-of-fit values ($\chi^2/d.o.f. = 7.7,\ 7.3,\ 6.0$ for MW, LMC, and SMC dust, respectively, but in this case, the very flat intrinsic spectral slopes $\beta \approx 0.1 - 0.2$ additionally speak against MW and LMC dust being the correct solution. SMC dust once again yields acceptable results ($\beta_{RF09,SMC} = 0.419 \pm 0.084$, $A_{V,RF09,SMC} = 2.162 \pm 0.103$ mag). Even this result is not in agreement with the *uvw*1 detection, however.

Overall, while there is no strong evidence for one or another foreground extinction, the most logical solution is SF11 foreground extinction with additional moderately small SMC extinction in the host galaxy. High host-galaxy extinction such as in the RF09 case is also not supported by the relatively small equivalent width of the Na doublet at the host redshift (Malesani et al., in prep.).

3.3. *The afterglow of GRB 221009A in a global context - luminous but not intrinsically extraordinary*

With knowledge of the intrinsic extinction and the redshift, and using the method first presented in Kann et al. (2006), we are able to place the optical/NIR afterglow of GRB 221009A in the context of a large sample of GRB afterglows. The sample is compiled from Kann et al. (2006, 2010, 2011, Kann et al. 2023a,b in prep.). These afterglows have been corrected for individual Galactic foreground extinction, host-galaxy contribution (where known) and SN contribution at late times (where applicable).

The otherwise as-observed light curves are shown in Fig. 4. We highlight the afterglows of the two exceptional GRBs mentioned in the introduction. For one, the nearby but only moderately energetic GRB 030329, whose afterglow (e.g., Lipkin et al. 2004; Kann et al. 2006) remains the most well-observed until this day, and is seen to be brighter than all other afterglows in the sample at any given time. And secondly the afterglow of the extremely bright GRB 130427A (e.g., Vestrand et al. 2014; Perley et al. 2014, Kann et al. 2023b, in prep.), also among the brightest observed GRB afterglows and energetically more similar to GRB 221009A.

The placement of the afterglow of GRB 221009A depends on the MW foreground extinction correction.

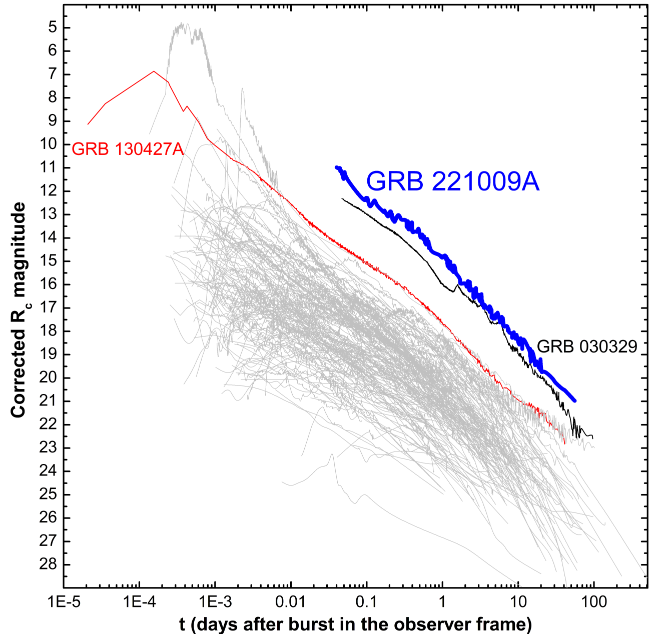

Figure 4. The afterglow light curve of GRB 221009A in context of a large sample of GRB afterglows (Kann et al. 2006, 2010, 2011, 2023a,b in prep.). These data have been corrected for Galactic extinction along each individual line-of-sight, and if possible for the host-galaxy and SN contribution. For the GRB 221009A afterglow, we show the result for SF11 Galactic extinction. We highlight the afterglows of two other GRBs, namely that of the much less energetic but similarly distant GRB 030329, and that of the well-studied, ultra-bright GRB 130427A, which had been the closest highly energetic ("cosmological") GRB so far. Assuming the higher extinction correction, the afterglow of GRB 221009A is seen to be the brightest that has ever been detected, even brighter than the afterglow of GRB 030329, however, by only a small margin.

From our three models, we display the SF11 solution here, which is usually the standard correction for extinction in other cases. If we use the MW-only solution, the resultant afterglow would be even brighter, whereas it would be magnitudes fainter with the RF09 solution, but as pointed out, this solution is unlikely. For SF11, we see the observed afterglow is even brighter than that of GRB 030329 at all times (albeit usually by not more than one magnitude) - potentially, yet another record that GRB 221009A holds. Williams et al. (2023) report the observed afterglow of GRB 221009A is by far the brightest X-ray afterglow, and also the brightest UVOT afterglow (after extinction correction) ever detected.

A better afterglow comparison can be achieved if we correct both for the distance (temporally and in terms of luminosity, we choose to place all afterglows at $z = 1$ and present them in the observer frame) as well as for any intrinsic (host-galaxy) extinction. If the latter

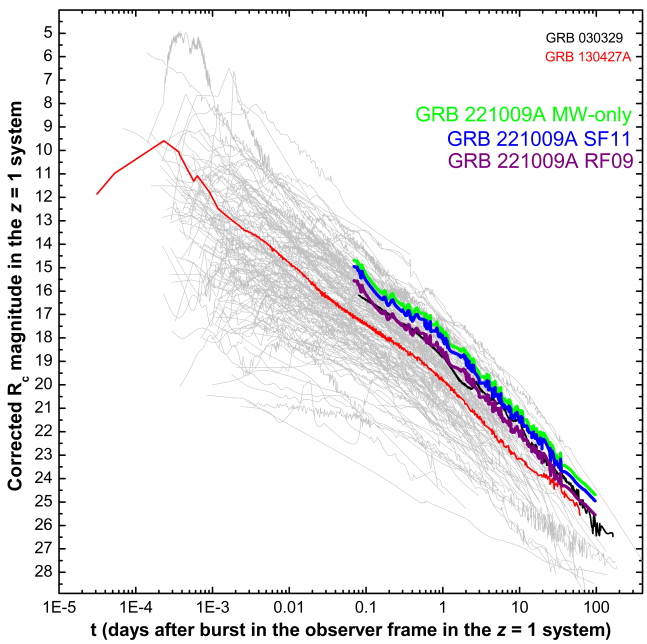

Figure 5. The same as Fig. 4, but now all afterglows are in the $z = 1$ system. This means that the afterglow magnitudes have been additionally corrected for host-galaxy extinction, and all of them have been shifted to $z = 1$ taking the individual spectral slopes β and cosmological k-correction into account. We again highlight the afterglows of the bright nearby GRBs 030329 and 130427A, and three solutions for GRB 221009A: The pure MW solution, SF11 MW extinction, and RF09 MW extinction along with the respective host-galaxy solutions. All yield similar brightness, and the afterglow is seen to be among the brighter ones detected so far. We note that the late afterglow of GRB 221009A is *not* corrected for host-galaxy and SN contributions and therefore the brightness is likely overestimated.

value is high, it can hide extremely luminous GRB afterglows from initially looking extraordinary (e.g., GRB 080607, Perley et al. 2011). The results are shown in Fig. 5. It can now be seen that the afterglow of GRB 130427A is only of medium brightness, and that of GRB 030329, while brighter, is also well within the sample of known afterglows. The same is true for the afterglow of GRB 221009A. The three foreground-extinction solutions yield similar results now, as high foreground extinction implies low additional host-galaxy extinction (MW-only, SF11), while the lower RF09 foreground extinction is mostly compensated by necessary high intrinsic extinction. For the favored SF11 extinction, the afterglow of GRB 221009A is clearly among the more luminous detected so far, but it is not egregious. Only at late times does the unbroken decay lead it to become exceptional, but we caution these observations are not corrected for host-galaxy and SN contribution and are therefore to be taken with caution (see Fulton et al. 2023 for the potential SN contribution, but see also Shrestha et al. 2023). Overall, despite its extreme energetics, the optical/NIR afterglow of GRB 221009A is not intrinsically extraordinary, a phenomenon also seen for other highly energetic GRBs like GRB 990123 (Kann et al. 2010). Williams et al. (2023) reach similar conclusions, for both the UVOT and the X-ray afterglow.

3.4. *Properties of the GRB afterglow from Bayesian Inference*

3.4.1. *Bayesian Inference using* `NMMA`*, investigation of the jet structure and SN contribution*

As a further framework to interpret GRB 221009A, we use the Nuclear physics and Multi-Messenger Astronomy framework `NMMA` (Dietrich et al. 2020; Pang et al. 2022)[14] that allows us to perform joint Bayesian inference of multi-messenger events containing gravitational waves, kilonovae, SNe, and GRB afterglows. For this work, we follow Kunert et al. (2023) and employ the top-hat jet structure and semi-analytic code `afterglowpy` (van Eerten et al. 2010; Ryan et al. 2020). In this model, the dynamics of the relativistic ejecta propagating through the interstellar medium are treated under the thin-shell approximation, and the angular structure is introduced by dissecting the blast wave into angular elements, each of which is evolved independently, including lateral expansion. Magnetic-field amplification, electron acceleration, and the synchrotron emission from the forward shock are treated according to the analytical prescriptions of Sari et al. (1998). The observed radiation is computed by performing equal-time arrival surface integration. It is important to note that the model does not account for the presence of the reverse shock or the early coasting phase, and it does not include inverse Compton radiation. This limits its applicability to the early afterglow of very bright GRBs. While we find possible evidence of an early reverse shock (or at least a brighter, more steeply decaying component; Laskar et al. 2023 state a reverse shock is not compatible with their radio emission), this phase is mapped by only a few data points and has little influence on the modeling.

For our analysis, we use the nested sampling algorithm implemented in PYMULTINEST (Buchner 2016) and employ X-ray measurements at 1 keV and 10 keV for XRT. For HXMT data, which span $1.5 - 10$ keV, we take it to be 5 keV. For the *Swift* X-ray data, we follow the procedure outlined in §2.1 and use only a resampled set of data points to avoid our Bayesian inference run being entirely dominated by X-ray observations without

[14] https://github.com/nuclear-multimessenger-astronomy/nmma

noticeable contributions from the observed data in the other bands. In the optical we use data in the u, b, g', V, r', R_C, i', I_C, and z' bands. The data are corrected for extinction using the two different assumptions for the foreground extinction, SF11 and RF09; cf. §3.2.

We present our best-fit light curves for the SF11 extinction and with/without the inclusion of the HXMT data in Fig. 6. Generally, we find that the observational data are well-recovered by the model, with differences that are noticeably smaller than the assumed 1 magnitude uncertainty of our model (shaded regions)[15].

Computing the log Bayes factor

$$\ln \mathcal{B}^{\rm SF11}_{\rm RF09} = \ln \frac{p(d|{\rm GRB}_{\rm model}, {\rm SF11})}{p(d|{\rm GRB}_{\rm model}, {\rm RF09})} \tag{1}$$

for our two extinctions of SF11 vs. RF09, we obtain 0.238 ± 0.095 when we do not include HXMT data and a log Bayes factor of SF11 against RF09 of 0.325 ± 0.097 if HXMT data are included, i.e., following Jeffrey's scale, we find that this difference is not statistically significant.

We present the corresponding source parameters, namely, the inclination angle $\theta_{\rm obs}$, isotropic energy E_0, the interstellar medium density $n_{\rm ism}$, half-opening angle of the jet core $\theta_{\rm core}$, and microphysical parameters $\{p, \epsilon_e, \epsilon_B\}$ (the power-law index of the electron energy distribution as well as the fractions of energy in electrons and the magnetic field, respectively) using the four different sets of data inside Fig. 7; each simulation uses 2048 live points for the nested sampling.

In general, we find consistent results within statistical uncertainties (quoted and shown at the 90% credible level) larger than the differences caused by the input data when analyzing the four data sets. Most surprising in our analysis might be the relatively large jet-opening angle (the viewing angle being near the edge but still within the jet), which might be hard to explain given the high isotropic energy release of the GRB. We find that for $\iota \approx 0$, the light curve seems to be dimmer than expected for the u-band data, which drives the analysis to prefer larger inclination angles. However, this early u-band data may contain a contribution from another emitting component, as discussed above. Nevertheless, considering that the lower bound of the posterior does reach values of a few degrees and that the inclusion of the 1 magnitude uncertainty generally leads to wider, less restrictive posteriors, we find consistent results with other analyses performed in this article and also previously shown in the literature, e.g., Laskar et al. (2023).

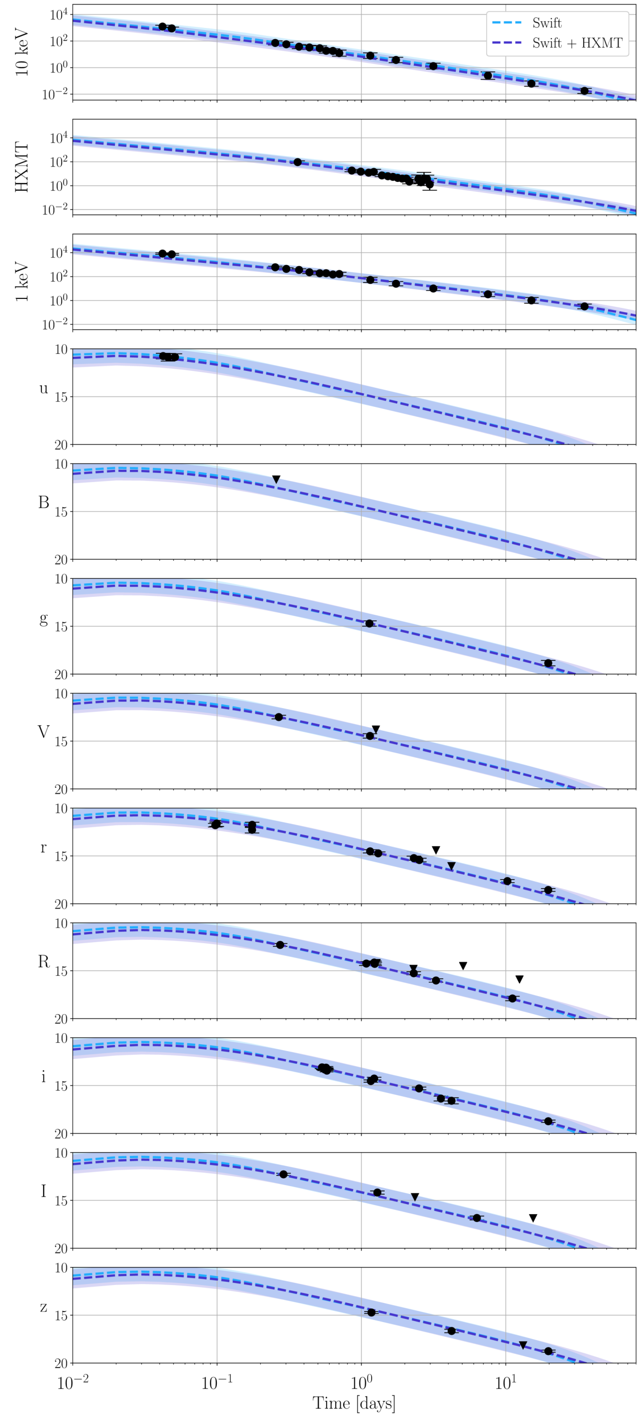

Figure 6. `NMMA` - Observational data and best-fit light curves for the NMMA analysis using the SF11 extinction and the two employed data sets (only *Swift* and *Swift* + HXMT data). Within the 1 magnitude uncertainty that we assume for our model, the observational data are recovered well. The X-ray bands are shown in μJy and the rest of the bands are shown in AB magnitude.

[15] Similar to Pang et al. (2022), this 1 magnitude uncertainty is included in the likelihood calculations.

The clear relation between $\theta_{\rm core}$ and $\theta_{\rm obs}$ seen in the posterior (Fig. 7) is attributed to the absence of the jet break in the present data.

The advantage of the NMMA framework is also the possibility to compare different astrophysical scenarios and models in a straightforward way. As a starting point, we compare different jet structures. In addition to the top-hat jet for which we showed results before, we also employed a Gaussian jet, which features an angular dependence $E(\theta_{\rm obs}) \propto \exp(-\theta_{\rm obs}^2/(2\theta_c^2))$ for $\theta_{\rm obs} \leq \theta_w$, with θ_w being an additional free parameter, and a power-law jet in which the energy scales as $E(\theta_{\rm obs}) \propto (1 + (\theta_{\rm obs}/\theta_c)^2/b)^{-b/2}$ for $\theta_{\rm obs} \leq \theta_w$, with b being an additional parameter. For simplicity, we restrict this comparison to the full *Swift* and HXMT data set and the SF11 extinction. Overall, we do not find strong statistical evidence for the presence of jet structure and the top-hat jet model remains preferred (due to the Occam's razor penalty to more complicated models).

Finally, following the study of Fulton et al. (2023), we investigate the possibility of a SN connected to GRB 221009A, which is not readily visible in the light curve. For modeling the SN, we use the `nugent-hyper` model from `sncosmo` (Levan et al. 2005) with a shift in the absolute magnitude, $S_{\rm max}$, as the main free parameter. We vary this free parameter within $S_{\rm max} \in [-30 \text{ mag}, 30 \text{ mag}]$. The nugent-hyper model is a template constructed from observations of SN 1998bw. Within our analysis, we find that in our runs combining the GRB top-hat jet afterglow with a SN component, the maximum log-likelihood slightly increases compared to the pure top-hat jet model to -108.88. Nevertheless, the log Bayes Factor prefers the simpler top-hat jet model and is 0.472 ± 0.098. Hence, despite this slight preference, there is no strong evidence for or against the presence of a SN contribution that would be described through the nugent-hyper model, consistent with other analyses, e.g., Shrestha et al. (2023).

3.4.2. *Limitations of `NMMA` and investigation of SSC emission using the IAP model*

Some of the parameters obtained with the aforementioned fits and presented in Fig. 7 are unusual for a typical GRB afterglow. Perhaps the most striking is the very large jet opening angle. It is constrained to $\theta_{\rm core} \gtrsim 10^\circ$, while typical jets have opening angles $\theta_{\rm core} \simeq (2.5 \pm 1.0)^\circ$ (Wang et al. 2018). This effect is mostly due to the absence of a clear jet break in the afterglow data up to 20 days, which is challenging to reproduce in a top-hat forward shock emission scenario, where we expect the jet break to be observed at $t_{\rm dec,obs} \propto (E_0/n_{\rm ism})^{1/3}\theta_{\rm core}^{8/3}$, for a constant density medium and an on-axis observer. A very late-time jet break naturally implies a combination of large opening angle, energy, and low medium density (De Pasquale et al. 2016). In Fig. 8, we show lines of constant jet break observation time $t_{\rm obs,dec} = 20$ days for several values of $n_{\rm ism}$ spanning our prior limits. Knowing that the energy dissipated during the prompt phase is at least $E_{\gamma,\rm iso} = 2 \times 10^{54}$ erg, and imposing a prompt efficiency of less than 50%, the initial energy $E_0 > E_{\gamma,\rm iso}$. If we assume this value for E_0, and enforce a low opening angle ($\theta_{\rm core} < 5^\circ$), $n_{\rm ism} < 10^{-6}$ cm^{-3} is extremely low. Conversely, if wider jet opening angles are allowed, this density can be increased. Still, the high ISM densities favored by our analysis remain challenging to reconcile with such a late-time jet break. If the jet break occurs before the first observations at $\sim 5 \times 10^{-2}$ days, a similar study leads to exceptionally low jet opening angles, or E_0. In either case, this characteristic of the afterglow is challenging to model.

To further validate the previous analysis, we also model the afterglow data of GRB 221009A using another model developed at IAP assuming synchrotron and Synchrotron Self-Compton (SSC) radiation at the forward shock of a relativistic blast wave propagating through the ISM. In this model, SSC diffusions can occur in both Thomson and Klein-Nishina regimes and are treated as first introduced in Nakar et al. (2009). This model also accounts for the jet lateral structure and any viewing angle, although in this case we do not include any lateral structure and fix the viewing angle $\theta_{\rm obs} = 0^\circ$. We also assume a constant-density ISM. Another difference with `afterglowpy` used in `NMMA` is that this model also includes the treatment of the coasting phase which can induce differences at early times, though an analysis with the best-fit parameters shows it does not impact the light curves in this case. A detailed model description will be provided provided in Pellouin & Daigne (2023).

We used a Markov Chain Monte Carlo (MCMC) routine to infer the physical parameters for the afterglow, using the optical data with SF11 extinction, as well as the HXMT X-ray data between 1.5 and 10 keV. For the χ^2 computation, we slightly modify the errors to avoid any over-fitting of points with very small errors, using $\max\{\text{flux error}; 0.3\times\text{flux}\}$. All data points are jointly fitted. We initialize 50 independent chains, and run them over 20000 iterations. After checking the convergence speed, we remove the first 2500 iterations as burn-in in the final results.

Our first analysis uses a simplified model where only synchrotron radiation powers the afterglow emission, for comparison with the analysis presented in §3.4.1. The posterior samples converge towards parameter values that are very similar to those presented in §3.4.1. Those values are listed in Table 2, and the results are presented in Fig. 9.

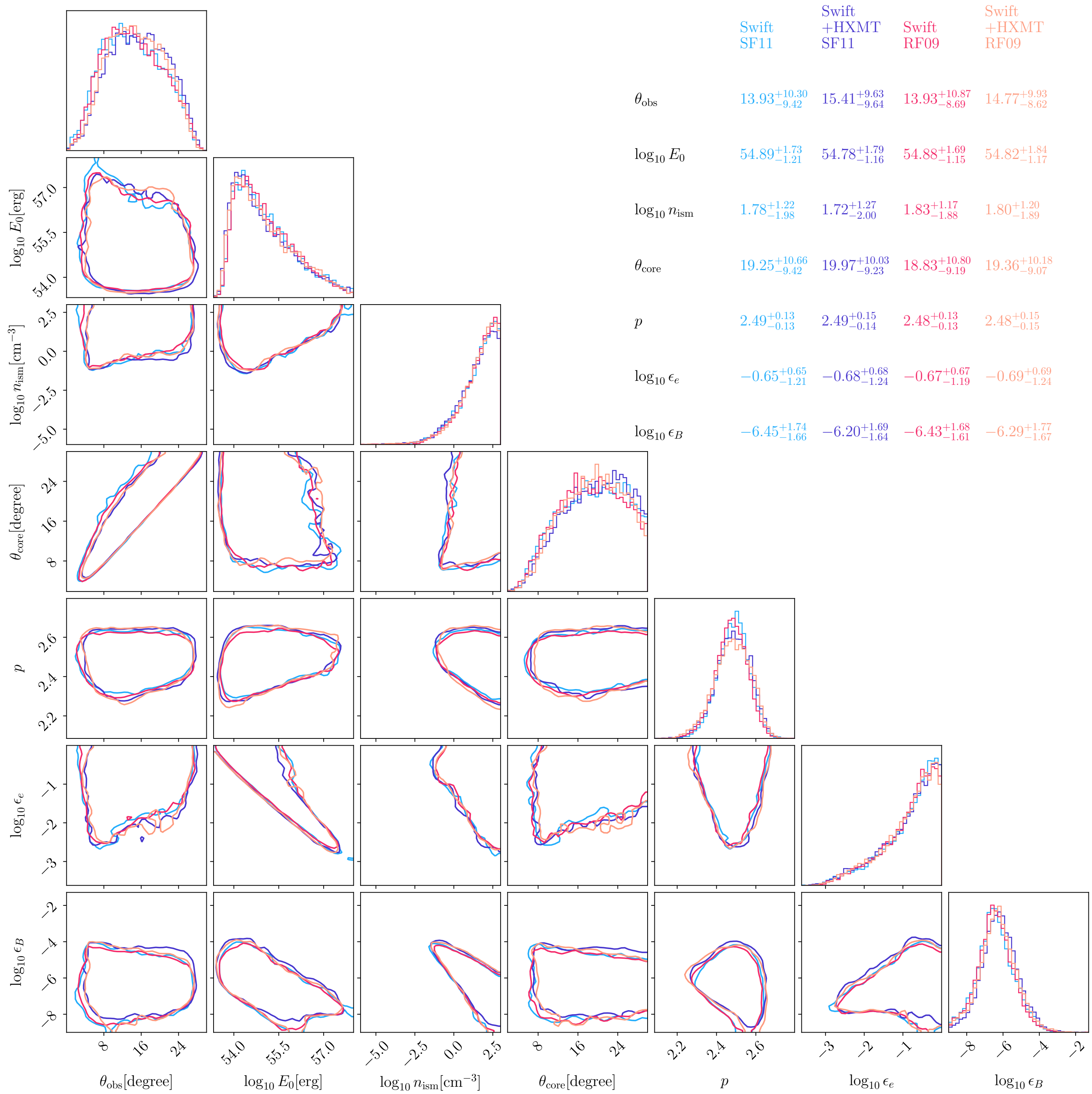

Figure 7. `NMMA` - Posterior distribution (shown are 90% confidence intervals) for our selected data sets when using the top-hat jet model of **`afterglowpy`**. Overall, we find consistent posteriors for different input data.

We also fit the data including both synchrotron and SSC components to see if this additional spectral component can help the parameter inference towards more realistic values. In this case, the posterior sample reaches extremely high values of E_0 close to our prior bounds (typically $E_0 \sim 10^{57} - 10^{58}$ erg). ϵ_e and ϵ_B have lower values and p is higher than in the synchrotron case. Other parameters have similar values. We find that a significant fraction of the synchrotron radiation budget is upscattered by SSC, hence such a high value for E_0. Once again, some posterior parameters have extreme values, hinting that these models suffer a lack of precision. Although as discussed in §3.4.1, the addition of a lateral structure does not seem to help the fit, the consideration of a wind-like medium could significantly change the results.

Table 1. `NMMA` - Parameters and prior bounds employed in our Bayesian inferences. We report median posterior values at 90 % credibility from simulations that were run with a top-hat jet structure using SF11 extinction with HXMT data for analysis, see §3.4.1 and Figs. 6,7. The ratio $\theta_{\rm obs}/\theta_{\rm core}$ is not directly sampled but derived from other parameters.

Parameter	Symbol	Bounds	Prior	Posterior
Isotropic afterglow energy [erg]	E_0	[10^{50},10^{58}]	log-uniform	$10^{54.78^{+1.73}_{-1.21}}$
Density of the ambient medium [$\rm cm^{-3}$]	$n_{\rm ism}$	[10^{-6},10^{3}]	log-uniform	$10^{1.72^{+1.27}_{-2.00}}$
Fraction of the energy which accelerates the electrons	$\epsilon_{\rm e}$	[10^{-4},1]	log-uniform	$10^{-0.68^{+0.68}_{-1.24}}$
Fraction of the energy which generates the magnetic field	$\epsilon_{\rm B}$	[10^{-9},1]	log-uniform	$10^{-6.20^{+1.69}_{-1.24}}$
Electron distribution power-law index	p	[2,3]	uniform	$2.49^{+0.15}_{-0.14}$
Opening angle of the jet core [degrees]	$\theta_{\rm core}$	[0.5,30]	uniform	$19.97^{+10.03}_{-9.23}$
Viewing angle [degrees]	$\theta_{\rm obs}$	[0.5,30]	uniform	$15.41^{+9.63}_{-9.64}$
Ratio of viewing angle to opening angle of jet core	$\theta_{\rm obs}/\theta_{\rm core}$	[1/60, 60],	-	$0.82^{+0.16}_{-0.20}$

Table 2. IAP model Bayesian Inference - Parameters and prior bounds employed in our Bayesian inferences. We report median posterior values at 90 % credibility from simulations that were run with a top-hat jet structure using SF11 extinction with HXMT data for the analysis presented in §3.4.2 and Fig. 9. We fixed the luminosity distance to $D_{\rm L}$ = 742 Mpc and the viewing angle to $\theta_{\rm obs} = 0°$.

Parameter	Symbol	Bounds	Prior	Posterior
Isotropic afterglow energy [erg]	E_0	[10^{50},10^{58}]	log-uniform	$10^{54.36^{+0.80}_{-0.53}}$
Initial Lorentz factor	Γ_0	[10^{1},10^{3}]	log-uniform	$10^{2.64^{+0.26}_{-0.38}}$
Density of the ambient medium [$\rm cm^{-3}$]	$n_{\rm ism}$	[10^{-6},10^{3}]	log-uniform	$10^{2.39^{+0.43}_{-0.67}}$
Fraction of the energy which accelerates the electrons	$\epsilon_{\rm e}$	[10^{-4},1]	log-uniform	$10^{-0.88^{+0.49}_{-0.75}}$
Fraction of the energy which generates the magnetic field	$\epsilon_{\rm B}$	[10^{-9},1]	log-uniform	$10^{-6.27^{+0.51}_{-0.45}}$
Fraction of electrons accelerated at the shock	ζ	[10^{-4},1]	log-uniform	$10^{-0.60^{+0.42}_{-0.63}}$
Electron population Lorentz factor injection index	p	[2,3]	uniform	$2.61^{+0.04}_{-0.04}$
Opening angle of the core of the jet [deg]	$\theta_{\rm core}$	[0.5,30]	uniform	$25.01^{+3.61}_{-6.19}$

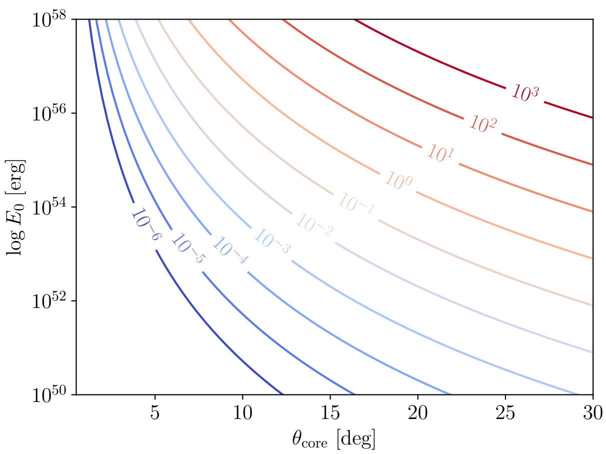

Figure 8. Lines of observed deceleration time at $t_{\rm obs,dec}$ = 20 days. Each colored line corresponds to a given ISM density $n_{\rm ism}$ in $\rm cm^{-3}$, which is labeled on the figure.

4. DISCUSSION AND CONCLUSION

In this work, the properties of the GRB 221009A afterglow are studied using a multi-wavelength data set, presenting data from optical observations from ground-based telescopes of the GRANDMA/KNC network and the Low Energy X-ray telescope (LE) onboard the *Insight*-HXMT satellite. The X-ray observations were made 9.8 hours to 3 days after the trigger time, while the ultraviolet, optical, and near-infrared sky was covered from the prompt emission (shallow limits from all-sky cameras) and then (with narrow-field instruments) from 2.2 hours after the trigger time to about 20 days. The GRANDMA network involved more than 30 telescopes, including both professional and amateur telescopes, and collected more than 200 images for this GRB. This is one of the few GRB afterglows that has been observed extensively by amateur astronomers. The measurements with the deepest limiting magnitudes reach $m_{lim} = 24.6$ mag in g' band by a professional telescope (CFHT) and $m_{lim} = 21.5$ mag in the V band by an amateur telescope, demonstrating the potential for citizen contribu-

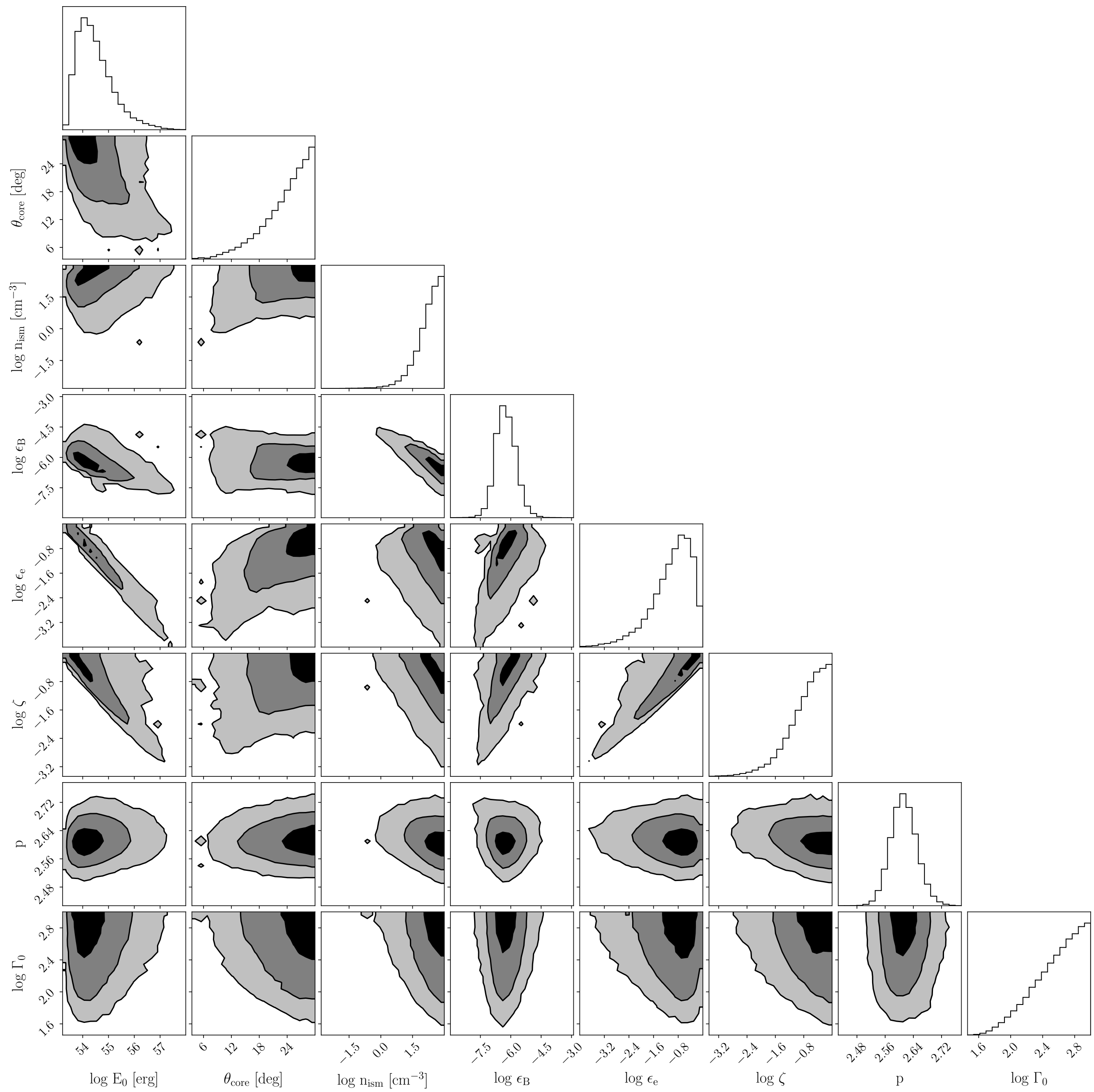

Figure 9. IAP model Bayesian Inference - Marginalized posterior distribution and correlation of the free parameters best fitting the joint optical and HXMT data with an on-axis observation of a top-hat jet radiating via synchrotron only, as presented in §3.4.2. The median values and 90% credible intervals are shown in Table 2. The contours represent the 1σ, 2σ and 3σ confidence regions.

tions to time-domain astrophysical science. We also collected prompt observations of the GRB in the optical (between T_0 and to T_0+500 seconds) by cameras managed by the Desert Fireball Network, but no optical flash was detected in the V band (down to a limiting magnitude of 3.8 mag). We furthermore collect public data from the XRT telescope onboard the *Swift* satellite, with the first observation having been taken about one hour after the GRB trigger time. Two specially-tuned photometric pipelines, STDPipe and Muphoten, are used to analyze the GRB afterglow data. The observations are calibrated using stars from the PS1 catalog; slightly different results being obtained for Johnson-Cousins filters between the two pipelines. For this reason, only a subset of data with good quality and consistent results have been selected for analysis.

In this paper, we tackle the challenge of determining the significant extinction correction, as the GRB lies behind the Galactic plane. To correct for this, we employ two different techniques: firstly, we use the SF11 maps (Schlafly & Finkbeiner 2011), which may overestimate the extinction. Secondly, we use the RF09 maps by Rowles & Froebrich (2009), which utilize near-infrared color excess determinations based on 2MASS observations. This method results in a significantly lower extinction value of $A_V = 2.195/E_{(B-V)} = 0.709$ mag (but is only valid out to $2-3$ kpc), compared to the SF11 value of $A_V = 4.1/E_{(B-V)} = 1.32$ mag. Taking into account the existence of dust at larger distances determined by X-ray measurements of dust rings (Negro et al. 2023; Vasilopoulos et al. 2023; Williams et al. 2023), we proceed to discuss the reliability of these measurements and conduct our follow-up analysis using both correction methods for comparison.

Empirical analysis of the light curve shows it to be composed of three power-law sections (steep, shallow, steep), with the first section only covered by a short data baseline. The data after ~ 0.1 d show a clear break and a relatively shallow post-break slope with no further indication of a jet break, which would usually lead to a decay slope $\alpha \gtrsim 2$. The light curve analysis yields a SED which we fit with three solutions for the foreground/host-galaxy extinction including one under the assumption that the entire extinction is foreground. All extinction models yield viable solutions; in combination with spectroscopic evidence for small-to-moderate host-galaxy extinction, we prefer the combination of SF11 foreground correction and about half a magnitude of SMC-type host-galaxy extinction. Using these values, we are able to compare the optical afterglow to a global sample and find it to be luminous but not excessively so, in contrast to the extreme isotropic energy release of the prompt emission, a result also found for the X-ray afterglow (Williams et al. 2023).

We perform a Bayesian Inference analysis to interpret the GRB afterglow using multi-wavelength light curves. We utilize the Nuclear physics and Multi-mMssenger Astronomy framework, `NMMA` (Dietrich et al. 2020; Pang et al. 2022), employing the semi-analytic code `afterglowpy` for light-curve generation. However, this analysis has some limitations, such as the absence of modeling of the reverse shock or the early coasting phase, and the lack of accounting for inverse Compton radiation. To minimize the influence of over-sampled X-ray data from *Swift* XRT, we re-sampled these data sets. Our results find consistency between those obtained using SF11 or RF09 extinctions, whether we considered all of our selected UVOIR data, combined with *Swift* XRT and/or HXMT data.

We conduct a study of the source parameter properties of GRB 221009A and its jet, finding a relatively large jet-opening angle, which is unexpected given the high isotropic energy release of the GRB. This result likely stems from the early u-band excess, as well as the assumption of a 1 magnitude uncertainty in the light curves, allowing for more parameter uncertainty. Another factor that might explain the results is the absence of a jet break in the available data. A large opening angle and a low $n_{\rm ism}$ would favour a late-time jet break, whereas a low viewing angle and a high $n_{\rm ism}$ would lead to an early-time jet break. Our analysis favours models with a large jet opening angle and a large $n_{\rm ism}$ and challenges the absence of a clear jet break in the data. An early-time jet break seems also unlikely given the very slow decay α in the early optical observations. There is also no strong statistical evidence for the presence of jet structure, and the simple top-hat jet model appears to be preferred as the GRB is viewed on-axis. Another possibility would be a very late-time jet break that naturally implies a combination of large opening angle, energy, and low circumburst medium density, which goes against another unusual result that we find, a *high* circumburst medium density. In order to validate our findings, we utilize another model proposed by Pellouin & Daigne (2023) that takes into consideration synchrotron and SSC radiation at the forward shock of a relativistic blast wave. Our analysis is restricted to the data sample collected from the HXMT, *Swift* UVOT and GRANDMA observatories. To check consistency with previous studies, we initially employ a simplified version of the model where only synchrotron emission powers the jet radiation. Subsequently, we add the SSC component and find that a considerable portion of the synchrotron radiation is upscattered by the SSC process, resulting in a high, and unrealistic, value of E_0.

Additionally, we investigate the possibility of a SN associated with GRB 221009A. Although a late-time bump in the light curve would be expected in this scenario, we do not observe such a bump (see also Shrestha et al. 2023). We used the `nugent-hyper` model from `sncosmo` to explore this possibility, but the maximum log-likelihood only slightly increases with the addition of the SN component. The log Bayes Factor, however, prefers the simpler top-hat jet model, so our analysis is not able to provide conclusive evidence for or against the presence of a SN contribution. Further analysis is required with a complete, multi-wavelength data set (including late-time observations in X-rays and radio) to differentiate between models, including the inherent jet structure, a potential jet break and the presence or absence of a SN. Despite the general afterglow structure being very simple, GRB 221009A still has many secrets that need to be uncovered in future works.

GRB 221009A is an absolutely unique event, representing not just the nearest extremely energetic GRB, but potentially also the most energetic GRB ever detected. These two factors combined make it by far the brightest GRB ever seen, at the very least a once-in-a-lifetime event, more probably even a millenial one. To have such an event occur when we have a fleet of satellites in space able to detect gamma-rays, and the ground- and space-based capabilities to determine the distance and follow up the afterglow evolution in detail, even by amateur astronomers, is fortuitous indeed. It is unlikely that a chance like this will come again in the coming decades or even centuries, making this an event to be remembered through the ages.

The GRANDMA consortium thanks the amateur participants of the Kilonova-Catcher program and observers from GRANDMA. GRANDMA thanks the paper writing team managed by D. A. Kann. The Kilonova-Catcher program is supported by the IdEx Université de Paris Cité, ANR-18-IDEX-0001. The GRANDMA collaboration thanks G. Parent, E. Maris, F. Bayard, O. Aguerre and M. Richmond for their observations. This project has received financial support from the CNRS through the MITI interdisciplinary programs. We thank Mathias Schultheis for fruitful discussions regarding extinction selection. D. A. Kann acknowledges the support by the State of Hessen within the Research Cluster ELEMENTS (Project ID 500/10.006). S. Antier acknowledges the financial support of the Programme National Hautes Energies (PNHE) and of Crédits Scientifiques Incitatifs d'UCA 2023. M. W. Coughlin acknowledges support from the National Science Foundation with grant numbers PHY-2010970 and OAC-2117997. C. Andrade and M. W. Coughlin were supported by the Preparing for Astrophysics with LSST Program, funded by the Heising Simons Foundation through grant 2021-2975, and administered by Las Cumbres Observatory. J.-G. Ducoin is supported by a research grant from the Ile-de-France Region within the framework of the Domaine d'Intérêt Majeur-Astrophysique et Conditions d'Apparition de la Vie (DIM-ACAV). This work has made use of the Infinity Cluster hosted by Institut d'Astrophysique de Paris. C. Pellouin acknowledges funding support from the Initiative Physique des Infinis (IPI), a research training program of the Idex SUPER at Sorbonne Université. The Egyptian team acknowledges support from the Science, Technology & Innovation Funding Authority (STDF) under grant number 45779. S. Karpov is supported by European Structural and Investment Fund and the Czech Ministry of Education, Youth and Sports (Project CoGraDS – CZ.02.1.01/0.0/0.0/15_003/0000437). J. Mao is supported by the NSFC 11673062 and Oversea Talent Program of Yunnan Province. The *Insight*-HXMT team acknowledges support from the National Key R&D Program of China (2021YFA0718500) and the National Natural Science Foundation of China under Grants Nos. U1838201, U1838202.

REFERENCES

Abbott, B. P., Abbott, R., Abbott, T. D., et al. 2017a, PhRvL, 119, 161101, doi: 10.1103/PhysRevLett.119.161101

—. 2017b, ApJL, 848, L12, doi: 10.3847/2041-8213/aa91c9

—. 2017c, ApJL, 848, L13, doi: 10.3847/2041-8213/aa920c

Ackermann, M., Ajello, M., Asano, K., et al. 2014, Science, 343, 42, doi: 10.1126/science.1242353

Aguerre, O., Bayard, F., Broens, E., et al. 2022, GRB Coordinates Network, 32934

Agüí Fernández, J. F., Thöne, C. C., Kann, D. A., et al. 2021, MNRAS, in press, arXiv:2109.13838. https://arxiv.org/abs/2109.13838

Ahumada, T., Singer, L. P., Anand, S., et al. 2021, Nature Astronomy, 5, 917, doi: 10.1038/s41550-021-01428-7

Ai, S., & Gao, H. 2022, arXiv e-prints, arXiv:2210.14116, doi: 10.48550/arXiv.2210.14116

Aivazyan, V., Almualla, M., Antier, S., et al. 2022, MNRAS, 515, 6007, doi: 10.1093/mnras/stac2054

Akerlof, C., Balsano, R., Barthelmy, S., et al. 1999, Nature, 398, 400, doi: 10.1038/18837

Almeida, A., Anderson, S. F., Argudo-Fernández, M., et al. 2023, arXiv e-prints, arXiv:2301.07688, doi: 10.48550/arXiv.2301.07688

Antier, S., Agayeva, S., Aivazyan, V., et al. 2020a, MNRAS, 492, 3904, doi: 10.1093/mnras/stz3142

Antier, S., Agayeva, S., Almualla, M., et al. 2020b, MNRAS, 497, 5518, doi: 10.1093/mnras/staa1846

Atri, P., An, T., Giroletti, M., et al. 2022, GRB Coordinates Network, 32907

Atteia, J. L. 2022, GRB Coordinates Network, 32793

Atteia, J. L., Heussaff, V., Dezalay, J. P., et al. 2017, ApJ, 837, 119, doi: 10.3847/1538-4357/aa5ffa

Atwood, W. B., Abdo, A. A., Ackermann, M., et al. 2009, ApJ, 697, 1071, doi: 10.1088/0004-637X/697/2/1071

Barthelmy, S. D., Barbier, L. M., Cummings, J. R., et al. 2005, SSRv, 120, 143, doi: 10.1007/s11214-005-5096-3

Becker, A. 2015, HOTPANTS: High Order Transform of PSF ANd Template Subtraction. http://ascl.net/1504.004

Belkin, S., Kim, V., Pozanenko, A., et al. 2022a, GRB Coordinates Network, 32769

Belkin, S., Moskvitin, A., Kim, V., et al. 2022b, GRB Coordinates Network, 32818

Belkin, S., Pozanenko, A., Klunko, E., Pankov, N., & GRB IKI FuN. 2022c, GRB Coordinates Network, 32645

Berger, E. 2014, ARA&A, 52, 43, doi: 10.1146/annurev-astro-081913-035926

Bertin, E. 2010, SWarp: Resampling and Co-adding FITS Images Together, Astrophysics Source Code Library, record ascl:1010.068. http://ascl.net/1010.068

Bertin, E. 2011, in Astronomical Society of the Pacific Conference Series, Vol. 442, Astronomical Data Analysis Software and Systems XX, ed. I. N. Evans, A. Accomazzi, D. J. Mink, & A. H. Rots, 435

Bertin, E., & Arnouts, S. 1996, A&AS, 117, 393, doi: 10.1051/aas:1996164

Bikmaev, I., Khamitov, I., Irtuganov, E., et al. 2022a, GRB Coordinates Network, 32743

—. 2022b, GRB Coordinates Network, 32752

Bissaldi, E., Omodei, N., Kerr, M., & Fermi-LAT Team. 2022, GRB Coordinates Network, 32637

Bloom, J. S., Perley, D. A., Li, W., et al. 2009, ApJ, 691, 723, doi: 10.1088/0004-637X/691/1/723

Boch, T., Fernique, P., Bonnarel, F., et al. 2020, in Astronomical Society of the Pacific Conference Series, Vol. 527, Astronomical Society of the Pacific Conference Series, ed. R. Pizzo, E. R. Deul, J. D. Mol, J. de Plaa, & H. Verkouter, 121

Boch, T., Pineau, F., & Derriere, S. 2012, in Astronomical Society of the Pacific Conference Series, Vol. 461, Astronomical Data Analysis Software and Systems XXI, ed. P. Ballester, D. Egret, & N. P. F. Lorente, 291

Boër, M., Atteia, J. L., Damerdji, Y., et al. 2006, ApJL, 638, L71, doi: 10.1086/501048

Bradley, L., Sipőcz, B., Robitaille, T., et al. 2021, astropy/photutils: 1.1.0, 1.1.0, Zenodo, doi: 10.5281/zenodo.4624996

Brivio, R., Ferro, M., D'Avanzo, P., et al. 2022, GRB Coordinates Network, 32652

Broens, E. 2022, GRB Coordinates Network, 32640

Buchner, J. 2016, PyMultiNest: Python interface for MultiNest, Astrophysics Source Code Library, record ascl:1606.005. http://ascl.net/1606.005

Burrows, D. N., Hill, J. E., Nousek, J. A., et al. 2005, SSRv, 120, 165, doi: 10.1007/s11214-005-5097-2

Cano, Z., Wang, S.-Q., Dai, Z.-G., & Wu, X.-F. 2017, Advances in Astronomy, 2017, 8929054, doi: 10.1155/2017/8929054

Cardelli, J. A., Clayton, G. C., & Mathis, J. S. 1989, ApJ, 345, 245, doi: 10.1086/167900

Castro-Tirado, A. J., Sanchez-Ramirez, R., Hu, Y. D., et al. 2022, GRB Coordinates Network, 32686

Chambers, K. C., Magnier, E. A., Metcalfe, N., et al. 2016, arXiv e-prints, arXiv:1612.05560. https://arxiv.org/abs/1612.05560

Chen, T. W., Malesani, D. B., Yang, S., et al. 2022, GRB Coordinates Network, 32667

D'Avanzo, P., Ferro, M., Brivio, R., et al. 2022, GRB Coordinates Network, 32755

De Pasquale, M., Page, M. J., Kann, D. A., et al. 2016, MNRAS, 462, 1111, doi: 10.1093/mnras/stw1704

de Ugarte Postigo, A., Izzo, L., Pugliese, G., et al. 2022, GRB Coordinates Network, 32648

de Wet. 2022, GRB Coordinates Network, 32944 de Wet, S., Groot, P. J., & Meerlicht Consortium. 2022, GRB Coordinates Network, 32646

Dichiara, S., Gropp, J. D., Kennea, J. A., et al. 2022a, The Astronomer's Telegram, 15650

—. 2022b, GRB Coordinates Network, 32632

Dietrich, T., Coughlin, M. W., Pang, P. T. H., et al. 2020, Science, 370, 1450, doi: 10.1126/science.abb4317

Duan, K.-K., Xu, Z.-L., Shen, Z.-Q., et al. 2022, GRB Coordinates Network, 32973

Durbak, J. M., Kutyrev, A. S., Andreoni, I., et al. 2022, GRB Coordinates Network, 32654

Duverne, P. A., Antier, S., Basa, S., et al. 2022, PASP, 134, 114504, doi: 10.1088/1538-3873/ac9c31

Dzhappuev, D. D., Afashokov, Y. Z., Dzaparova, I. M., et al. 2022, The Astronomer's Telegram, 15669

Evans, P. A., Beardmore, A. P., Page, K. L., et al. 2007, A&A, 469, 379, doi: 10.1051/0004-6361:20077530

—. 2009, MNRAS, 397, 1177, doi: 10.1111/j.1365-2966.2009.14913.x

Ferro, M., Brivio, R., D'Avanzo, P., et al. 2022, GRB Coordinates Network, 32804

Frederiks, D., Lysenko, A., Ridnaia, A., et al. 2022, GRB Coordinates Network, 32668

Froebrich, D., Ray, T. P., Murphy, G. C., & Scholz, A. 2005, A&A, 432, L67, doi: 10.1051/0004-6361:200500016

Fulton, M. D., Smartt, S. J., Rhodes, L., et al. 2023, arXiv e-prints, arXiv:2301.11170, doi: 10.48550/arXiv.2301.11170

Ge, M. Y., Chen, Y. P., Liao, J. Y., et al. 2022, The Astronomer's Telegram, 15703

Gehrels, N., Ramirez-Ruiz, E., & Fox, D. B. 2009, ARA&A, 47, 567, doi: 10.1146/annurev.astro.46.060407.145147

Gehrels, N., Chincarini, G., Giommi, P., et al. 2004, ApJ, 611, 1005, doi: 10.1086/422091

Gehrels, N., Barthelmy, S. D., Burrows, D. N., et al. 2008, ApJ, 689, 1161, doi: 10.1086/592766

Gendre, B., Stratta, G., Atteia, J. L., et al. 2013, ApJ, 766, 30, doi: 10.1088/0004-637X/766/1/30

GLAST Facility Science Team, Gehrels, N., & Michelson, P. 1999, Astroparticle Physics, 11, 277, doi: 10.1016/S0927-6505(99)00066-3

Goldstein, A., Veres, P., Burns, E., et al. 2017, ApJL, 848, L14, doi: 10.3847/2041-8213/aa8f41

Gotz, D., Mereghetti, S., Savchenko, V., et al. 2022, GRB Coordinates Network, 32660

Greiner, J., Klose, S., Reinsch, K., et al. 2003, Nature, 426, 157, doi: 10.1038/nature02077

Groot, P. J., Vreeswijk, P. M., Ter Horst, R., et al. 2022, GRB Coordinates Network, 32678

Guha, A., & Nicholson, P. 2022, GRB Coordinates Network, 32745

Gupta, R., Ror, A. K., Pandey, S. B., et al. 2022, GRB Coordinates Network, 32811

Hayes, L. A., & Gallagher, P. T. 2022, Research Notes of the American Astronomical Society, 6, 222, doi: 10.3847/2515-5172/ac9d2f10.48550/arXiv.2210.15284

Hjorth, J., & Bloom, J. S. 2012, in Chapter 9 in "Gamma-Ray Bursts" (Cambridge University Press), 169–190

Hjorth, J., Sollerman, J., Møller, P., et al. 2003, Nature, 423, 847, doi: 10.1038/nature01750

Hou, L. G., & Han, J. L. 2014, A&A, 569, A125, doi: 10.1051/0004-6361/20142403910.48550/arXiv.1407.7331

Hu, Y. D., Casanova, V., Fernandez-Garcia, E., et al. 2022, GRB Coordinates Network, 32644

Huang, Y., Hu, S., Chen, S., et al. 2022, GRB Coordinates Network, 32677

Huber, M., Schultz, A., Chambers, K. C., et al. 2022, GRB Coordinates Network, 32758

IceCube Collaboration. 2022, GRB Coordinates Network, 32665

Iwakiri, W., Jaisawal, G. K., Younes, G., et al. 2022, GRB Coordinates Network, 32694

Izzo, L., Saccardi, A., Fynbo, J. P. U., et al. 2022, GRB Coordinates Network, 32765

Jin, Z.-P., Zhou, H., Wang, Y., et al. 2023, arXiv e-prints, arXiv:2301.02407. https://arxiv.org/abs/2301.02407

Kann, D. A., & Agui Fernandez, J. F. 2022, GRB Coordinates Network, 32762

Kann, D. A., Klose, S., & Zeh, A. 2006, ApJ, 641, 993, doi: 10.1086/500652

Kann, D. A., Masetti, N., & Klose, S. 2007, AJ, 133, 1187, doi: 10.1086/511066

Kann, D. A., Klose, S., Zhang, B., et al. 2010, ApJ, 720, 1513, doi: 10.1088/0004-637X/720/2/1513

—. 2011, ApJ, 734, 96, doi: 10.1088/0004-637X/734/2/96

Karpov, S. 2021, STDPipe: Simple Transient Detection Pipeline. http://ascl.net/2112.006

Kennea, J. A., Williams, M., & Swift Team. 2022a, GRB Coordinates Network, 32635

Kennea, J. A., Tohuvavohu, A., Osborne, J. P., et al. 2022b, GRB Coordinates Network, 32651

Kim, V., Krugov, M., Pozanenko, A., et al. 2022, GRB Coordinates Network, 32670

KM3NeT Collaboration. 2022, GRB Coordinates Network, 32741

Kobayashi, K., Negoro, H., Nakajima, M., et al. 2022, GRB Coordinates Network, 32756

Kobayashi, S. 2000, ApJ, 545, 807, doi: 10.1086/317869

Kostov, A., & Bonev, T. 2018, Bulgarian Astronomical Journal, 28, 3, doi: 10.48550/arXiv.1706.06147
Kouveliotou, C., Meegan, C. A., Fishman, G. J., et al. 1993, ApJL, 413, L101, doi: 10.1086/186969
Kulkarni, S. R., Djorgovski, S. G., Odewahn, S. C., et al. 1999, Nature, 398, 389, doi: 10.1038/18821
Kumar, H., Swain, V., Waratkar, G., et al. 2022, GRB Coordinates Network, 32662
Kunert, N., Antier, S., Nedora, V., et al. 2023, arXiv e-prints, arXiv:2301.02049, doi: 10.48550/arXiv.2301.02049
Lapshov, I., Molkov, S., Mereminsky, I., et al. 2022, GRB Coordinates Network, 32663
Laskar, T., Alexander, K. D., Margutti, R., et al. 2023, arXiv e-prints, arXiv:2302.04388. https://arxiv.org/abs/2302.04388
Lesage, S., Veres, P., Roberts, O. J., et al. 2022, GRB Coordinates Network, 32642
Levan, A., Nugent, P., Fruchter, A., et al. 2005, ApJ, 624, 880, doi: 10.1086/428657
Levan, A. J., Tanvir, N. R., Starling, R. L. C., et al. 2014a, ApJ, 781, 13, doi: 10.1088/0004-637X/781/1/13
Levan, A. J., Tanvir, N. R., Fruchter, A. S., et al. 2014b, ApJ, 792, 115, doi: 10.1088/0004-637X/792/2/115
Lipkin, Y. M., Ofek, E. O., Gal-Yam, A., et al. 2004, ApJ, 606, 381, doi: 10.1086/383000
Liu, J. C., Zhang, Y. Q., Xiong, S. L., et al. 2022, GRB Coordinates Network, 32751
Mao, J., Lu, K. X., Zhao, X. H., & Bai, J. M. 2022, GRB Coordinates Network, 32727
Maselli, A., Melandri, A., Nava, L., et al. 2014, Science, 343, 48, doi: 10.1126/science.1242279
Matheson, T., Garnavich, P. M., Stanek, K. Z., et al. 2003, ApJ, 599, 394, doi: 10.1086/379228
Mazets, E. P., Golenetskii, S. V., Ilinskii, V. N., et al. 1981, Ap&SS, 80, 3, doi: 10.1007/BF00649140
Meegan, C., Lichti, G., Bhat, P. N., et al. 2009, ApJ, 702, 791, doi: 10.1088/0004-637X/702/1/791
Melandri, A., Pian, E., D'Elia, V., et al. 2014, A&A, 567, A29, doi: 10.1051/0004-6361/201423572
Minaev, P. Y., & Pozanenko, A. S. 2020, MNRAS, 492, 1919, doi: 10.1093/mnras/stz3611
Mitchell, L. J., Phlips, B. F., & Johnson, W. N. 2022, GRB Coordinates Network, 32746
Mösta, P., Ott, C. D., Radice, D., et al. 2015, Nature, 528, 376, doi: 10.1038/nature15755
Nakar, E. 2007, PhR, 442, 166, doi: 10.1016/j.physrep.2007.02.005
Nakar, E., Ando, S., & Sari, R. 2009, ApJ, 703, 675, doi: 10.1088/0004-637X/703/1/675
Neckel, T., & Klare, G. 1980, A&AS, 42, 251
Negoro, H., Nakajima, M., Kobayashi, K., et al. 2022, The Astronomer's Telegram, 15651
Negro, M., Di Lalla, N., Omodei, N., et al. 2023, arXiv e-prints, arXiv:2301.01798. https://arxiv.org/abs/2301.01798
Nysewander, M., Fruchter, A. S., & Pe'er, A. 2009, ApJ, 701, 824, doi: 10.1088/0004-637X/701/1/824
O'Connor, B., Cenko, S. B., Troja, E., et al. 2022a, GRB Coordinates Network, 32739
—. 2022b, GRB Coordinates Network, 32799
O'Connor, B., Troja, E., Dichiara, S., Gillanders, J., & Cenko, S. B. 2022c, GRB Coordinates Network, 32750
—. 2022d, GRB Coordinates Network, 32860
Odeh, M. 2022, GRB Coordinates Network, 32649
Omodei, N., Bruel, P., Bregeon, J., et al. 2022a, GRB Coordinates Network, 32760
—. 2022b, GRB Coordinates Network, 32916
Paek, G. S. H., Im, M., Urata, Y., & Sung, H.-I. 2022, GRB Coordinates Network, 32659
Pal, S., Hobara, Y., Shvets, A., et al. 2023, Atmosphere, 14, 217, doi: 10.3390/atmos14020217
Pancino, E., Marrese, P. M., Marinoni, S., et al. 2022, A&A, 664, A109, doi: 10.1051/0004-6361/202243939
Pang, P. T. H., Dietrich, T., Coughlin, M. W., et al. 2022, arXiv e-prints, arXiv:2205.08513, doi: 10.48550/arXiv.2205.08513
Pannarale, F. 2022, GRB Coordinates Network, 32877
Pei, Y. C. 1992, ApJ, 395, 130, doi: 10.1086/171637
Pellouin, C., & Daigne, F. 2023, *in prep.*
Perley, D. A., Morgan, A. N., Updike, A., et al. 2011, AJ, 141, 36, doi: 10.1088/0004-6256/141/2/36
Perley, D. A., Cenko, S. B., Corsi, A., et al. 2014, ApJ, 781, 37, doi: 10.1088/0004-637X/781/1/37
Piano, G., Verrecchia, F., Bulgarelli, A., et al. 2022, GRB Coordinates Network, 32657
Pillera, R., Bissaldi, E., Omodei, N., et al. 2022, GRB Coordinates Network, 32658
Pineau, F.-X., Boch, T., Derrière, S., & Schaaff, A. 2020, in Astronomical Society of the Pacific Conference Series, Vol. 522, Astronomical Data Analysis Software and Systems XXVII, ed. P. Ballester, J. Ibsen, M. Solar, & K. Shortridge, 125
Popowski, P., Cook, K. H., & Becker, A. C. 2003, AJ, 126, 2910, doi: 10.1086/37929110.48550/arXiv.astro-ph/0303075
Racusin, J. L., Karpov, S. V., Sokolowski, M., et al. 2008, Nature, 455, 183, doi: 10.1038/nature07270
Rajabov, Y., Sadibekova, T., Tillayev, Y., et al. 2022, GRB Coordinates Network, 32795

Rastinejad, J., & Fong, W. 2022, GRB Coordinates Network, 32749

Rastinejad, J. C., Gompertz, B. P., Levan, A. J., et al. 2022, Nature, 612, 223, doi: 10.1038/s41586-022-05390-w

Ripa, J., Pal, A., Werner, N., et al. 2022, GRB Coordinates Network, 32685

Romanov, F. 2022a, arXiv e-prints, arXiv:2212.12543, doi: 10.48550/arXiv.2212.12543

Romanov, F. D. 2022b, GRB Coordinates Network, 32664

—. 2022c, GRB Coordinates Network, 32679

Roming, P. W. A., Kennedy, T. E., Mason, K. O., et al. 2005, SSRv, 120, 95, doi: 10.1007/s11214-005-5095-4

Rossi, A., Rothberg, B., Palazzi, E., et al. 2022, ApJ, 932, doi: 10.3847/1538-4357/ac60a2

Rowles, J., & Froebrich, D. 2009, MNRAS, 395, 1640, doi: 10.1111/j.1365-2966.2009.14655.x

Ryan, G., van Eerten, H., Piro, L., & Troja, E. 2020, Astrophys. J., 896, 166, doi: 10.3847/1538-4357/ab93cf

Sari, R., & Piran, T. 1999, ApJ, 520, 641, doi: 10.1086/307508

Sari, R., Piran, T., & Narayan, R. 1998, Astrophys. J. Lett., 497, L17, doi: 10.1086/311269

Sasada, M., Imai, Y., Murata, K. L., et al. 2022, GRB Coordinates Network, 32730

Schlafly, E. F., & Finkbeiner, D. P. 2011, ApJ, 737, 103, doi: 10.1088/0004-637X/737/2/103

Schlegel, D. J., Finkbeiner, D. P., & Davis, M. 1998, ApJ, 500, 525, doi: 10.1086/305772

Schneider, B., Adami, C., Le Floc'h, E., et al. 2022, GRB Coordinates Network, 32753

Schnoor, P. W., Nicholson, P., & Welch, D. L. 2022, GRB Coordinates Network, 32744

Selsing, J., Malesani, D., Goldoni, P., et al. 2019, A&A, 623, A92, doi: 10.1051/0004-6361/201832835

Shresta, M., Sand, D., Alexander, K. D., et al. 2022, GRB Coordinates Network, 32759

Shrestha, M., Bostroem, K., Sand, D., et al. 2022, GRB Coordinates Network, 32771

Shrestha, M., Sand, D. J., Alexander, K. D., et al. 2023, arXiv e-prints, arXiv:2302.03829. https://arxiv.org/abs/2302.03829

Stanek, K. Z., Matheson, T., Garnavich, P. M., et al. 2003, ApJL, 591, L17, doi: 10.1086/376976

Strausbaugh, R. 2022a, GRB Coordinates Network, 32693

—. 2022b, GRB Coordinates Network, 32738

Tan, W. J., Li, C. K., Ge, M. Y., et al. 2022, The Astronomer's Telegram, 15660

Thöne, C. C., Greiner, J., Savaglio, S., & Jehin, E. 2007, ApJ, 671, 628, doi: 10.1086/522558

Thöne, C. C., de Ugarte Postigo, A., Fryer, C. L., et al. 2011, Nature, 480, 72, doi: 10.1038/nature10611

Tiengo, A., Pintore, F., Mereghetti, S., Salvaterra, R., & a larger Collaboration. 2022, GRB Coordinates Network, 32680

Tohuvavohu, A., Beardmore, A. P., Osborne, J. P., et al. 2022, GRB Coordinates Network, 32671

Tonry, J. L., Stubbs, C. W., Lykke, K. R., et al. 2012, ApJ, 750, 99, doi: 10.1088/0004-637X/750/2/99

Towner, M. C., Cupak, M., Deshayes, J., et al. 2020, PASA, 37, e008, doi: 10.1017/pasa.2019.48

Troja, E., Fryer, C. L., O'Connor, B., et al. 2022, Nature, 612, 228, doi: 10.1038/s41586-022-05327-3

Ursi, A., Panebianco, G., Pittori, C., et al. 2022, GRB Coordinates Network, 32650

van der Horst, A. J., Paragi, Z., de Bruyn, A. G., et al. 2014, MNRAS, 444, 3151, doi: 10.1093/mnras/stu1664

van Eerten, H., Leventis, K., Meliani, Z., Wijers, R., & Keppens, R. 2010, Mon. Not. Roy. Astron. Soc., 403, 300, doi: 10.1111/j.1365-2966.2009.16109.x

Vanderspek, R., Sakamoto, T., Barraud, C., et al. 2004, ApJ, 617, 1251, doi: 10.1086/423923

Vasilopoulos, G., Karavola, D., Stathopoulos, S. I., & Petropoulou, M. 2023, MNRAS, doi: 10.1093/mnras/stad375

Veres, P., Burns, E., Bissaldi, E., et al. 2022, GRB Coordinates Network, 32636

Vestrand, W. T., Wren, J. A., Panaitescu, A., et al. 2014, Science, 343, 38, doi: 10.1126/science.1242316

Vidal, E., Zheng, W., Filippenko, A. V., & KAIT GRB team. 2022, GRB Coordinates Network, 32669

Vinko, J., Bodi, A., Pal, A., et al. 2022, GRB Coordinates Network, 32709

Wang, X.-G., Zhang, B., Liang, E.-W., et al. 2018, ApJ, 859, 160, doi: 10.3847/1538-4357/aabc13

Williams, M. A., Kennea, J. A., Dichiara, S., et al. 2023, arXiv e-prints, arXiv:2302.03642. https://arxiv.org/abs/2302.03642

Woosley, S. E. 1993, ApJ, 405, 273, doi: 10.1086/172359

Xia, Z.-Q., Wang, Y., Yuan, Q., & Fan, Y.-Z. 2022a, GRB Coordinates Network, 32748

—. 2022b, arXiv e-prints, arXiv:2210.13052, doi: 10.48550/arXiv.2210.13052

Xu, D., Jiang, S. Q., Fu, S. Y., et al. 2022, GRB Coordinates Network, 32647

Yang, J., Ai, S., Zhang, B.-B., et al. 2022, Nature, 612, 232, doi: 10.1038/s41586-022-05403-8

Zhang, B. B., Liu, Z. K., Peng, Z. K., et al. 2021, Nature Astronomy, 5, 911, doi: 10.1038/s41550-021-01395-z

Zhang, S.-N., Li, T., Lu, F., et al. 2020, Science China Physics, Mechanics, and Astronomy, 63, 249502, doi: 10.1007/s11433-019-1432-6

Table 3. Data used for the numerical data analysis sections (§3.4.1, §3.4.2). *Swift* data have been converted from the Vega system to the AB system. Data are given fully extinction-corrected, for either SF11 MW foreground extinction, or RF09, and the corresponding SMC extinction in the host galaxy (§3.2).

Delay		Filter	SF11		RF09		Observatory
(day)	(sec)		Magnitude	Upper-limit	Magnitude	Upper-limit	
0.0423	3.657×10^3	u	10.76 ± 0.29	-	10.65 ± 0.35	-	*Swift* UVOT
0.0457	3.949×10^3	u	10.88 ± 0.40	-	10.77 ± 0.44	-	*Swift* UVOT
0.0511	4.416×10^3	u	10.86 ± 0.34	-	10.75 ± 0.39	-	*Swift* UVOT
0.2572	2.222×10^4	B	-	11.66	-	11.69	KNC-SCT-0.28
1.1368	9.822×10^4	g'	14.71 ± 0.28	-	14.70 ± 0.31	-	KAO
19.6945	1.702×10^6	g'	18.85 ± 0.28	-	18.84 ± 0.31	-	CFHT-Megacam
-0.0010	-90	V	-	-2.9	-	-2.9	Mundrabilla
-0.0007	-60	V	-	-2.9	-	-2.9	Mundrabilla
-0.0003	-30	V	-	-1.1	-	-1.1	Raw War Road
0.0000	0	V	-	-1.1	-	-1.1	Raw War Road
0.0004	30	V	-	-1.1	-	-1.1	Raw War Road
0.0007	60	V	-	-1.1	-	-1.1	Raw War Road
0.0011	90	V	-	-1.1	-	-1.1	Raw War Road
0.0014	120	V	-	-1.1	-	-1.1	Raw War Road
0.0017	150	V	-	-1.1	-	-1.1	Raw War Road
0.0021	180	V	-	-1.1	-	-1.1	Raw War Road
0.0024	210	V	-	-1.1	-	-1.1	Raw War Road
0.0031	270	V	-	-1.1	-	-1.1	Raw War Road
0.0035	300	V	-	-1.1	-	-1.1	Raw War Road
0.0042	360	V	-	-1.1	-	-1.1	Raw War Road
0.0045	390	V	-	-1.1	-	-1.1	Raw War Road
0.2677	2.313×10^4	V	12.49 ± 0.19	-	12.50 ± 0.22	-	KNC-SCT-0.28
1.1465	9.906×10^4	V	14.46 ± 0.23	-	14.47 ± 0.26	-	ShAO
1.2606	1.089×10^5	V	-	13.79	-	13.80	KNC-SCT-0.28
0.0972	8.40×10^3	r'	11.79 ± 0.19	-	11.79 ± 0.21	-	TRE
0.0993	8.58×10^3	r'	11.69 ± 0.23	-	11.69 ± 0.25	-	TRE
0.0995	8.60×10^3	r'	11.61 ± 0.32	-	11.61 ± 0.33	-	TRE
0.1748	1.510×10^4	r'	12.27 ± 0.33	-	12.27 ± 0.35	-	TRE
0.1750	1.512×10^4	r'	11.75 ± 0.27	-	11.75 ± 0.29	-	TRE
1.1489	9.926×10^4	r'	14.52 ± 0.17	-	14.52 ± 0.19	-	KAO
1.3077	1.130×10^5	r'	14.73 ± 0.15	-	14.73 ± 0.18	-	C2PU/Omicron
2.3083	1.994×10^5	r'	15.23 ± 0.21	-	15.23 ± 0.23	-	KNC-Parent
2.5206	2.178×10^5	r'	15.43 ± 0.19	-	15.43 ± 0.21	-	KNC-LCO/McDO-0.4m
3.2874	2.840×10^5	r'	-	14.27	-	14.27	KNC-C11-ATLAS
4.2097	3.637×10^5	r'	-	16.07	-	16.07	KAO
10.2667	8.870×10^5	r'	17.63 ± 0.16	-	17.63 ± 0.19	-	C2PU/Omicron
19.6965	1.702×10^6	r'	18.56 ± 0.15	-	18.56 ± 0.18	-	CFHT/MegaCam
0.2736	2.364×10^4	R_C	12.30 ± 0.15	-	12.34 ± 0.18	-	KNC-SCT-0.28
1.0813	9.342×10^4	R_C	14.25 ± 0.20	-	14.29 ± 0.22	-	UBAI-ST60
1.2274	1.060×10^5	R_C	14.14 ± 0.16	-	14.18 ± 0.19	-	Lisnyky AZT-8
1.2365	1.068×10^5	R_C	14.28 ± 0.16	-	14.32 ± 0.19	-	Lisnyky AZT-8
1.2755	1.102×10^5	R_C	-	14.19	-	14.23	KNC-SCT-0.28
2.2956	1.983×10^5	R_C	-	14.80	-	14.84	KNC-SCT-0.28

Table 3. Continued.

Delay (day)	Delay (sec)	Filter	SF11 Magnitude	SF11 Upper-limit	RF09 Magnitude	RF09 Upper-limit	Observatory
2.3042	1.991×10^5	R_C	15.26 ± 0.16	-	15.30 ± 0.19	-	Lisnyky AZT-8
3.2868	2.840×10^5	R_C	16.02 ± 0.18	-	16.06 ± 0.20	-	Lisnyky AZT-8
5.0674	4.378×10^5	R_C	-	14.50	-	14.54	UBAI-ST60
11.1313	9.617×10^5	R_C	17.90 ± 0.23	-	17.94 ± 0.25	-	UBAI-AZT22
12.4567	1.076×10^6	R_C	-	15.91	-	15.95	VIRT
1.1625	1.004×10^5	i'	14.53 ± 0.12	-	14.56 ± 0.14	-	KAO
1.2255	1.059×10^5	i'	14.27 ± 0.14	-	14.30 ± 0.16	-	KNC-IRIS
4.2108	3.638×10^5	i'	16.59 ± 0.32	-	16.62 ± 0.33	-	KAO
19.7097	1.703×10^6	i'	18.73 ± 0.12	-	18.76 ± 0.14	-	CFHT/MegaCam
0.2887	2.494×10^4	I_C	12.28 ± 0.11	-	12.21 ± 0.13	-	KNC-SCT-0.28
0.5333	4.608×10^4	I_C	13.10 ± 0.12	-	13.13 ± 0.14	-	KNC-BGO
0.5372	4.641×10^4	I_C	13.11 ± 0.12	-	13.14 ± 0.14	-	KNC-BGO
0.5411	4.675×10^4	I_C	13.14 ± 0.12	-	13.17 ± 0.14	-	KNC-BGO
0.5450	4.709×10^4	I_C	13.20 ± 0.12	-	13.23 ± 0.14	-	KNC-BGO
0.5489	4.742×10^4	I_C	13.24 ± 0.13	-	13.27 ± 0.15	-	KNC-BGO
0.5527	4.775×10^4	I_C	13.23 ± 0.12	-	13.26 ± 0.14	-	KNC-BGO
0.5572	4.814×10^4	I_C	13.32 ± 0.12	-	13.35 ± 0.14	-	KNC-BGO
0.5611	4.848×10^4	I_C	13.30 ± 0.12	-	13.33 ± 0.14	-	KNC-BGO
0.5650	4.882×10^4	I_C	13.27 ± 0.13	-	13.30 ± 0.15	-	KNC-BGO
0.5689	4.915×10^4	I_C	13.13 ± 0.12	-	13.16 ± 0.14	-	KNC-BGO
0.5727	4.948×10^4	I_C	13.30 ± 0.13	-	13.33 ± 0.15	-	KNC-BGO
0.5766	4.982×10^4	I_C	13.44 ± 0.13	-	13.47 ± 0.15	-	KNC-BGO
1.2902	1.115×10^5	I_c	14.18 ± 0.17	-	14.12 ± 0.18	-	KNC-SCT-0.28
2.3509	2.031×10^5	I_c	-	14.66	-	14.60	KNC-SCT-0.28
2.5092	2.168×10^5	I_C	15.30 ± 0.14	-	15.33 ± 0.16	-	KNC-BGO
3.5534	3.070×10^5	I_C	16.36 ± 0.25	-	16.39 ± 0.26	-	KNC-BGO
6.3104	5.452×10^5	I_c	16.84 ± 0.20	-	16.77 ± 0.21	-	Lisnyky AZT-8
15.4848	1.338×10^6	I_c	-	16.86	-	16.79	VIRT
1.1745	1.015×10^5	z'	14.72 ± 0.10	-	14.70 ± 0.11	-	KAO
4.217	3.643×10^5	z'	16.65 ± 0.18	-	16.63 ± 0.19	-	KAO
13.184	1.139×10^6	z'	-	18.15	-	18.13	KAO
19.7308	1.705×10^6	z'	18.76 ± 0.11	-	18.74 ± 0.12	-	CFHT/MegaCam

Delay (day)	Delay (sec)	X-ray Filter Central frequency	Flux (Jansky)	Flux error (Jansky)	Observatory
0.1644	1.420×10^4	3.5 keV	3.74×10^{-4}	7.49×10^{-5}	*HXMT*/LE
0.3617	3.125×10^4	3.5 keV	9.32×10^{-5}	2.06×10^{-5}	*HXMT*/LE
0.8580	7.413×10^4	3.5 keV	1.83×10^{-5}	3.66×10^{-6}	*HXMT*/LE
0.9896	8.550×10^4	3.5 keV	1.49×10^{-5}	2.99×10^{-6}	*HXMT*/LE
1.1223	9.697×10^4	3.5 keV	1.23×10^{-5}	2.45×10^{-6}	*HXMT*/LE
1.2192	1.053×10^5	3.5 keV	1.41×10^{-5}	5.53×10^{-6}	*HXMT*/LE
1.3864	1.198×10^5	3.5 keV	7.18×10^{-6}	1.44×10^{-6}	*HXMT*/LE
1.5256	1.318×10^5	3.5 keV	6.17×10^{-6}	1.23×10^{-6}	*HXMT*/LE
1.6526	1.428×10^5	3.5 keV	5.45×10^{-6}	1.09×10^{-6}	*HXMT*/LE
1.7844	1.542×10^5	3.5 keV	4.44×10^{-6}	8.87×10^{-7}	*HXMT*/LE
1.9157	1.655×10^5	3.5 keV	3.91×10^{-6}	7.82×10^{-7}	*HXMT*/LE
2.0485	1.770×10^5	3.5 keV	3.91×10^{-6}	8.87×10^{-7}	*HXMT*/LE
2.1473	1.855×10^5	3.5 keV	2.19×10^{-6}	7.59×10^{-7}	*HXMT*/LE
2.4809	2.143×10^5	3.5 keV	3.73×10^{-6}	1.93×10^{-6}	*HXMT*/LE
2.5822	2.231×10^5	3.5 keV	1.92×10^{-6}	3.84×10^{-7}	*HXMT*/LE
2.7138	2.345×10^5	3.5 keV	3.64×10^{-6}	2.62×10^{-6}	*HXMT*/LE
2.8464	2.459×10^5	3.5 keV	3.73×10^{-6}	3.83×10^{-6}	*HXMT*/LE
2.9744	2.570×10^5	3.5 keV	1.27×10^{-6}	8.57×10^{-7}	*HXMT*/LE

Table 3. Continued.

Delay (day)	(sec)	X-ray Filter Central frequency	Flux (Jansky)	Flux error (Jansky)	Observatory
0.0419	0.362×10^4	10 keV	1.23×10^{-3}	2.51×10^{-4}	*Swift* XRT
0.0486	0.420×10^4	10 keV	8.95×10^{-4}	1.88×10^{-4}	*Swift* XRT
0.2529	2.185×10^4	10 keV	7.23×10^{-5}	2.14×10^{-5}	*Swift* XRT
0.3018	2.608×10^4	10 keV	5.71×10^{-5}	1.64×10^{-5}	*Swift* XRT
0.3701	3.197×10^4	10 keV	3.76×10^{-5}	1.10×10^{-5}	*Swift* XRT
0.4365	3.771×10^4	10 keV	3.29×10^{-5}	9.87×10^{-6}	*Swift* XRT
0.5145	4.445×10^4	10 keV	2.87×10^{-5}	9.62×10^{-6}	*Swift* XRT
0.5698	4.923×10^4	10 keV	1.85×10^{-5}	6.31×10^{-6}	*Swift* XRT
0.6348	5.484×10^4	10 keV	1.80×10^{-5}	5.48×10^{-6}	*Swift* XRT
0.7026	6.070×10^4	10 keV	1.22×10^{-5}	4.97×10^{-6}	*Swift* XRT
1.1524	9.957×10^4	10 keV	7.96×10^{-6}	3.02×10^{-6}	*Swift* XRT
1.7367	1.500×10^5	10 keV	3.76×10^{-6}	1.41×10^{-6}	*Swift* XRT
3.1510	2.722×10^5	10 keV	1.30×10^{-6}	5.16×10^{-7}	*Swift* XRT
7.5292	6.505×10^5	10 keV	2.49×10^{-7}	1.19×10^{-7}	*Swift* XRT
15.060	1.301×10^6	10 keV	6.23×10^{-8}	2.32×10^{-8}	*Swift* XRT
35.155	3.038×10^6	10 keV	1.77×10^{-8}	6.24×10^{-9}	*Swift* XRT
0.0419	0.362×10^4	1 keV	8.36×10^{-3}	1.16×10^{-3}	*Swift* XRT
0.0486	0.420×10^4	1 keV	7.25×10^{-3}	1.04×10^{-3}	*Swift* XRT
0.2529	2.185×10^4	1 keV	5.98×10^{-4}	1.12×10^{-4}	*Swift* XRT
0.3018	2.608×10^4	1 keV	4.39×10^{-4}	8.75×10^{-5}	*Swift* XRT
0.3701	3.197×10^4	1 keV	3.59×10^{-4}	6.76×10^{-5}	*Swift* XRT
0.4365	3.771×10^4	1 keV	2.30×10^{-4}	5.15×10^{-5}	*Swift* XRT
0.5145	4.445×10^4	1 keV	1.89×10^{-4}	4.82×10^{-5}	*Swift* XRT
0.5698	4.923×10^4	1 keV	1.91×10^{-4}	4.60×10^{-5}	*Swift* XRT
0.6348	5.484×10^4	1 keV	1.49×10^{-4}	3.07×10^{-5}	*Swift* XRT
0.7026	6.070×10^4	1 keV	1.65×10^{-4}	4.62×10^{-5}	*Swift* XRT
1.1524	9.957×10^4	1 keV	5.23×10^{-5}	2.04×10^{-5}	*Swift* XRT
1.7367	1.500×10^5	1 keV	2.53×10^{-5}	8.48×10^{-6}	*Swift* XRT
3.1510	2.722×10^5	1 keV	1.01×10^{-5}	3.28×10^{-6}	*Swift* XRT
7.5292	6.505×10^5	1 keV	3.31×10^{-6}	1.18×10^{-6}	*Swift* XRT
15.060	1.301×10^6	1 keV	1.02×10^{-6}	4.32×10^{-7}	*Swift* XRT
35.155	3.038×10^6	1 keV	3.20×10^{-7}	1.17×10^{-7}	*Swift* XRT

Table 4. The GRANDMA and GCN optical observations of GRB 221009A. In column (2), the T_{mid} time is the delay between the beginning of the observation and the *Fermi* GBM GRB trigger time (2022-10-09T13:16:59.99) in days. In column (5), magnitudes are given in the AB system and not corrected for Galactic and host-galaxy dust extinction. In column (9), the VETO tag refers to GRANDMA data that were not analyzed due to the bad quality of the images.

T_{start} UT (1)	T_{mid} (days) MJD (2)	$T-T_{GRB}$ (2)	Filter (3)	Exposure (4)	Magnitude (5)	U.L. (6)	Telescope (7)	Reference (8)	Analysis method (9)
2022-10-09T18:06:27	59861.7545	0.2010	u'	6×60s	-	17.9 (3σ)	MeerLICHT	de Wet et al. (2022)	-
2022-10-10T05:00	59862.2083	0.6549	u'	6×60s	-	-	Nickel-1m	Vidal et al. (2022)	-
2022-10-09T19:19:51	59861.8107	0.2572	B	5×180s	-	18.1 (5σ)	KNC-SCT-0.28	Broens (2022) & this work	STDPIPE
2022-10-10T04:21	59862.1812	0.6278	B	5×60s	-	19.7	LOAO-1m	Paek et al. (2022)	-
2022-10-09T16:21	59861.6812	0.1278	g'	200s	17.66 ± 0.07	-	GIT	Kumar et al. (2022)	-
2022-10-09T18:21	59861.7646	0.2111	g'	6×60s	18.22 ± 0.33	-	MeerLICHT	de Wet et al. (2022)	-
2022-10-10T05:00	59862.2083	0.6549	g'	300s	18.96 ± 0.1	-	Nickel-1m	Vidal et al. (2022)	-
2022-10-10T11:39	59862.4854	0.932	g'	8340s	-	18.3	MITSuME	Sasada et al. (2022)	-
2022-10-10T12:25	59862.5174	0.9639	g'	2×150s	-	18.3 (3σ)	SLT-40	Chen et al. (2022)	-
2022-10-10T16:34	59862.6903	1.1368	g'	2×120s	20.38 ± 0.19	19.9 (3σ)	KAO	this work	MUPHOTEN
2022-10-10T16:56	59862.7056	1.1521	g'	600s	20.13 ± 0.08	-	RTT-150	Bikmaev et al. (2022a)	-
2022-10-10T17:16	59862.7194	1.166	g'	15×30s	20.53 ± 0.1	21.0 (3σ)	AZT-20	Belkin et al. (2022a)	-
2022-10-10T19:40	59862.8194	1.266	g'	3×100s	20.87 ± 0.36	-	LCOGT	Strausbaugh (2022a)	-
2022-10-10T20:17	59862.8451	1.2917	g'	600s	20.44 ± 0.25	-	RTT-150	Bikmaev et al. (2022a)	-
2022-10-11T17:10	59863.7153	2.1618	g'	600s	21.15 ± 0.21	-	RTT-150	Bikmaev et al. (2022a)	-
2022-10-12T02:40	59864.1111	2.5577	g'	-	-	23.0	LBTO	Shresta et al. (2022)	-
2022-10-12T03:34	59864.1486	2.5952	g'	3×300s	-	22.3	LCOGT	Strausbaugh (2022b)	-
2022-10-15T15:44	59867.6556	6.1021	g'	30×60s	22.6 ± 0.12	23.4(3σ)	AZT-20	Belkin et al. (2022a)	-
2022-10-29T05:57	59881.2479	19.6945	g'	3×300s	24.52 ± 0.2	26.1	CFHT-Megacam	this work	MUPHOTEN
2022-10-09T13:15:29	59861.5524	-0.0010	V	27s	-	2.0	Mundrabilla	this work	section 2.2
2022-10-09T13:15:59	59861.5528	-0.0007	V	27s	-	2.0	Mundrabilla	this work	section 2.2
2022-10-09T13:16:30	59861.5531	-0.0003	V	27s	-	3.8	RawWarRoad	this work	section 2.2
2022-10-09T13:17:00	59861.5535	0.0000	V	27s	-	3.8	RawWarRoad	this work	section 2.2
2022-10-09T13:17:30	59861.5538	0.0004	V	27s	-	3.8	RawWarRoad	this work	section 2.2
2022-10-09T13:18:00	59861.5542	0.0007	V	27s	-	3.8	RawWarRoad	this work	section 2.2
2022-10-09T13:18:30	59861.5545	0.0011	V	27s	-	3.8	RawWarRoad	this work	section 2.2
2022-10-09T13:19:00	59861.5549	0.0014	V	27s	-	3.8	RawWarRoad	this work	section 2.2
2022-10-09T13:19:30	59861.5552	0.0017	V	27s	-	3.8	RawWarRoad	this work	section 2.2
2022-10-09T13:20:00	59861.5556	0.0021	V	27s	-	3.8	RawWarRoad	this work	section 2.2
2022-10-09T13:20:30	59861.5559	0.0024	V	27s	-	3.8	RawWarRoad	this work	section 2.2
2022-10-09T13:21:30	59861.5566	0.0031	V	27s	-	3.8	RawWarRoad	this work	section 2.2
2022-10-09T13:22:00	59861.5569	0.0035	V	27s	-	3.8	RawWarRoad	this work	section 2.2
2022-10-09T13:23:00	59861.5576	0.0042	V	27s	-	3.8	RawWarRoad	this work	section 2.2
2022-10-09T13:23:30	59861.5580	0.0045	V	27s	-	3.8	RawWarRoad	this work	section 2.2
2022-10-09T19:35:00	59861.82118	0.2677	V	5×180s	17.39 ± 0.08	18.3 (5σ)	KNC-SCT-0.28	Broens (2022) & this work	MUPHOTEN
2022-10-10T04:23	59862.1826	0.6292	V	5×60s	18.74 ± 0.13	19.5	LOAO-1m	Paek et al. (2022)	-
2022-10-10T16:48	59862.7	1.1465	V	25×120s	19.36 ± 0.15	19.5	ShAOT60	this work	STDPIPE
2022-10-10T19:16	59862.8141	1.2606	V	11×180s	-	18.7 (5σ)	KNC-SCT-0.28	this work	MUPHOTEN
2022-10-14T20:13	59866.8768	5.3233	V	180×32s	21.55 ± 0.24	21.2 (5σ)	KNC-T-CAT	this work	STDPIPE
2022-10-09T19:51	59861.8271	0.2736	R_c	5×180s	16.26 ± 0.05	17.9 (5σ)	KNC-SCT-0.28	Broens (2022) & this work	MUPHOTEN
2022-10-10T11:39	59862.4854	0.932	R_c	60s	-	17.0	MITSuME	Sasada et al. (2022)	-
2022-10-10T14:56	59862.6347	1.0813	R_c	6×180s	18.21 ± 0.14	18.5	UBAI-ST60	this work	MUPHOTEN
2022-10-10T15:53	59862.6774	1.124	R_c	15×90s	-	-	ShAOT60	this work	VETO
2022-10-10T18:32	59862.7809	1.2274	R_c	25×30s	18.1 ± 0.08	19.3	Lisnyky-AZT-8	this work	MUPHOTEN
2022-10-10T18:45	59862.7899	1.2365	R_c	25×30s	18.24 ± 0.08	19.1	Lisnyky-AZT-8	this work	MUPHOTEN
2022-10-10T19:43:14	59862.8290	1.2755	R_c	7×180s	-	18.2 (5σ)	KNC-SCT-0.28	this work	MUPHOTEN
2022-10-11T19:52:44	59863.8292	2.2956	R_c	20×180s	-	18.8 (5σ)	KNC-SCT-0.28	Broens (2022) & this work	MUPHOTEN
2022-10-11T18:44	59863.8576	2.3042	R_c	111×60s	19.22 ± 0.08	20.5	Lisnyky-AZT-8	this work	MUPHOTEN
2022-10-12T14:24	59864.6139	3.0604	R_c	5×240s	-	-	UBAI-ST60	this work	VETO
2022-10-12T19:40	59864.8403	3.2868	R_c	30×60s	19.98 ± 0.11	20.1	Lisnyky-AZT-8	this work	MUPHOTEN
2022-10-14T14:10	59866.6208	5.0674	R_c	11×240s	-	18.5	UBAI-ST60	this work	MUPHOTEN
2022-10-21T22:58	59874.0102	12.4567	R_c	460×10s	-	19.9	VIRT	this work	MUPHOTEN
2022-10-22T03:34:20	59874.1697	12.6162	R_c	6×600 s	-	19.4 (5σ)	KNC-iT11	this work	STDPIPE
2022-10-09T14:25	59861.6007	0.0472	r'	-	14.93 ± 0.1	-	NEXT	Xu et al. (2022)	-
2022-10-09T14:27	59861.6021	0.0486	r'	120s	14.84 ± 0.09	20.8	Mondy	Belkin et al. (2022c)	-
2022-10-09T15:36	59861.6507	0.0972	r'	180s	15.92 ± 0.12	16.5	TRE	this work	STDPIPE & MUPHOTEN
2022-10-09T15:39	59861.6528	0.0993	r'	180s	15.82 ± 0.18	16.7	TRE	this work	STDPIPE & MUPHOTEN
2022-10-09T15:40	59861.6530	0.0995	r'	180s	15.74 ± 0.28	16.1	TRE	this work	STDPIPE & MUPHOTEN
2022-10-09T16:25	59861.684	0.1306	r'	200s	16.16 ± 0.07	-	GIT	Kumar et al. (2022)	-
2022-10-09T17:28	59861.7283	0.1748	r'	180s	16.4 ± 0.3	16.3	TRE	this work	STDPIPE & MUPHOTEN
2022-10-09T17:29	59861.7285	0.1750	r'	180s	15.88 ± 0.23	16.3	TRE	this work	STDPIPE & MUPHOTEN
2022-10-09T18:25	59861.7674	0.2139	r'	-	16.5 ± 0.1	-	NEXT	Xu et al. (2022)	-
2022-10-09T18:23	59861.766	0.2125	r'	6×60s	16.76 ± 0.08	-	MeerLICHT	de Wet (2022)	-
2022-10-09T18:49	59861.784	0.2306	r'	90s	16.57 ± 0.02	-	OSN-0.9	Hu et al. (2022)	-
2022-10-09T23:58	59861.9986	0.4452	r'	-	17.36 ± 0.12	-	REM	Brivio et al. (2022)	-
2022-10-10T04:25	59862.184	0.6306	r'	60×5s	17.55 ± 0.06	19.8	LOAO-1m	Paek et al. (2022)	-
2022-10-10T05:00	59862.2083	0.6549	r'	300s	17.8 ± 0.1	-	Nickel-1m	Vidal et al. (2022)	-

Table 4. Continued.

2022-10-10T12:25	59862.5174	0.9639	r'	2×150s	18.67 ± 0.16	-	SLT-40	Chen et al. (2022)	-
2022-10-10T16:33	59862.7023	1.1489	r'	11×100s	18.65 ± 0.08	20.9	KAO	this work	Muphoten
2022-10-10T17:06	59862.7125	1.159	r'	600s	18.65 ± 0.02	-	RTT-150	Bikmaev et al. (2022a)	-
2022-10-10T17:14	59862.7181	1.1646	r'	18×30s	18.64 ± 0.03	20.8 (3σ)	AZT-20	Kim et al. (2022)	-
2022-10-10T19:26	59862.8097	1.2563	r'	2×300s	18.74 ± 0.12	-	RC-80	Vinko et al. (2022)	-
2022-10-10T19:40	59862.8194	1.266	r'	3×100s	18.8 ± 0.21	-	LCOGT	Strausbaugh (2022a)	-
2022-10-10T20:30	59862.8611	1.3077	r'	2×300s	18.86 ± 0.04	20.5	C2PU/Omicron	this work	STDPipe & Muphoten
2022-10-10T20:50	59862.8681	1.3146	r'	600s	18.81 ± 0.05	-	RTT-150	Bikmaev et al. (2022a)	-
2022-10-11T00:15	59863.0444	1.4909	r'	16×360s	18.89 ± 0.06	20.4 (5σ)	KNC-C14/Ste-Sophie	this work	STDPipe
2022-10-11T00:58	59863.0846	1.5312	r'	59×120s	18.93 ± 0.09	19.8 (5σ)	KNC-C11-FREE	this work	STDPipe
2022-10-11T16:37	59863.6924	2.1389	r'	600s	19.53 ± 0.04	-	RTT-150	Bikmaev et al. (2022a)	-
2022-10-11T20:41	59863.8617	2.3083	r'	-	19.36 ± 0.15	19.8 (5σ)	KNC-Parent	this work	STDPipe
2022-10-11T20:44	59863.8639	2.3104	r'	600s	19.67 ± 0.11	-	RTT-150	Bikmaev et al. (2022a)	-
2022-10-12T01:36	59864.1041	2.5506	r'	31×180s	19.56 ± 0.12	20.2 (5σ)	KNC-LCO/McDO-0.4m	this work	STDPipe
2022-10-12T03:34	59864.1486	2.5952	r'	3×300s	-	21.4	LCOGT	Strausbaugh (2022b)	-
2022-10-12T17:05	59864.7118	3.1583	r'	600s	20.03 ± 0.06	-	RTT-150	Bikmaev et al. (2022a)	-
2022-10-12T17:38	59864.7347	3.1813	r'	600s	19.97 ± 0.08	-	RTT-150	Bikmaev et al. (2022a)	-
2022-10-12T18:10	59864.7569	3.2035	r'	600s	20.07 ± 0.19	-	RTT-150	Bikmaev et al. (2022a)	-
2022-10-12T18:42	59864.7792	3.2257	r'	600s	20.32 ± 0.17	-	RTT-150	Bikmaev et al. (2022a)	-
2022-10-12T19:15	59864.8409	3.2874	r'	30×120s	-	18.4	KNC-C11-ATLAS	this work	STDPipe
2022-10-12T19:46	59864.8236	3.2702	r'	600s	20.17 ± 0.12	-	RTT-150	Bikmaev et al. (2022a)	-
2022-10-12T19:40	59864.8194	3.266	r'	1800s	20.23 ± 0.09	-	OHP	Schneider et al. (2022)	-
2022-10-12T20:18	59864.8458	3.2924	r'	300s	20.58 ± 0.7	-	RC-80	Vinko et al. (2022)	-
2022-10-12T20:25	59864.8507	3.2972	r'	600s	20.26 ± 0.16	-	RTT-150	Bikmaev et al. (2022a)	-
2022-10-12T20:57	59864.8729	3.3195	r'	600s	20.24 ± 0.19	-	RTT-150	Bikmaev et al. (2022a)	-
2022-10-13T03:09	59865.1312	3.5778	r'	-	20.44 ± 0.05	-	LDT	O'Connor et al. (2022a)	-
2022-10-13T17:37	59865.7632	4.2097	r'	21×120s	-	20.2	KAO	this work	Muphoten
2022-10-13T16:53	59865.7035	4.15	r'	600s	20.53 ± 0.09	-	RTT-150	Bikmaev et al. (2022b)	-
2022-10-13T17:25	59865.7257	4.1722	r'	600s	20.63 ± 0.09	-	RTT-150	Bikmaev et al. (2022b)	-
2022-10-13T17:58	59865.7486	4.1952	r'	600s	20.71 ± 0.15	-	RTT-150	Bikmaev et al. (2022b)	-
2022-10-13T18:30	59865.7708	4.2174	r'	600s	20.54 ± 0.1	-	RTT-150	Bikmaev et al. (2022b)	-
2022-10-13T19:02	59865.7931	4.2396	r'	600s	20.55 ± 0.12	-	RTT-150	Bikmaev et al. (2022b)	-
2022-10-13T19:35	59865.816	4.2625	r'	600s	20.74 ± 0.16	-	RTT-150	Bikmaev et al. (2022b)	-
2022-10-13T20:08	59865.8389	4.2854	r'	600s	20.9 ± 0.23	-	RTT-150	Bikmaev et al. (2022b)	-
2022-10-13T20:43	59865.8632	4.3097	r'	600s	20.86 ± 0.27	-	RTT-150	Bikmaev et al. (2022b)	-
2022-10-14T05:27	59866.2271	4.6736	r'	-	20.92 ± 0.05	-	Pan-STARRS	Huber et al. (2022)	-
2022-10-15T14:40	59867.6111	6.0577	r'	30×60s	20.96 ± 0.05	22.9 (3σ)	AZT-20	Belkin et al. (2022a)	-
2022-10-15T06:34	59867.2736	5.7202	r'	-	21.13 ± 0.06	-	Faulkes	Shrestha et al. (2022)	-
2022-10-16T14:41	59868.6118	7.0583	r'	200×25s	21.3 ± 0.04	-	DFOT	Gupta et al. (2022)	-
2022-10-19T02:05	59871.0868	9.5333	r'	-	21.68 ± 0.07	-	LDT	O'Connor et al. (2022b)	-
2022-10-19T18:26	59871.8201	10.2667	r'	4×300s	21.8 ± 0.07	21.9	C2PU/Omicron	this work	STDPipe & Muphoten
2022-10-20T16:11	59872.6847	11.1313	r'	3×300s	21.86 ± 0.18	21.8	UBAI-AZT22	this work	Muphoten
2022-10-21T14:33	59873.6062	12.0528	r'	30×60s	21.94 ± 0.07	23.9(3σ)	AZT-20	Belkin et al. (2022b)	-
2022-10-23T00:59:10	59875.0757	13.5222	r'	31×180s	-	19.4 (5σ)	KNC-C11-FREE	this work	STDPipe
2022-10-25T01:59:52	59877.1045	15.5510	r'	6×600s	-	20.5 (5σ)	KNC-iT11	this work	STDPipe
2022-10-27T00:45:41	59879.0501	17.4967	r'	26×120s	-	20.0 (5σ)	KNC-C11-FREE	this work	STDPipe
2022-10-29T05:50	59881.25	19.6965	r'	2×300s	22.69 ± 0.05	25.5	CFHT-Megacam	this work	STDPipe & Muphoten
2022-10-09T18:26:56	59861.7687	0.2152	i'	6×60s	15.58 ± 0.03	-	MeerLICHT	de Wet et al. (2022)	-
2022-10-10T02:04:32	59862.0868	0.5333	i'	300s	16.24 ± 0.05	17.9 (5σ)	KNC-BGO	this work	STDPipe
2022-10-10T02:10:06	59862.0907	0.5372	i'	300s	16.25 ± 0.05	17.9 (5σ)	KNC-BGO	this work	STDPipe
2022-10-10T02:15:41	59862.0945	0.5411	i'	300s	16.28 ± 0.05	17.9 (5σ)	KNC-BGO	this work	STDPipe
2022-10-10T02:21:15	59862.0984	0.5450	i'	300s	16.34 ± 0.05	17.9 (5σ)	KNC-BGO	this work	STDPipe
2022-10-10T02:26:50	59862.1023	0.5489	i'	300s	16.38 ± 0.06	17.8 (5σ)	KNC-BGO	this work	STDPipe
2022-10-10T02:32:25	59862.1062	0.5527	i'	300s	16.37 ± 0.05	17.9 (5σ)	KNC-BGO	this work	STDPipe
2022-10-10T02:38:55	59862.1107	0.5572	i'	300s	16.46 ± 0.05	18.0 (5σ)	KNC-BGO	this work	STDPipe
2022-10-10T02:44:29	59862.1107	0.5611	i'	300s	16.44 ± 0.05	17.9 (5σ)	KNC-BGO	this work	STDPipe
2022-10-10T02:50:04	59862.1184	0.5650	i'	300s	16.41 ± 0.06	17.9 (5σ)	KNC-BGO	this work	STDPipe
2022-10-10T02:55:39	59862.1223	0.5689	i'	300s	16.27 ± 0.05	17.8 (5σ)	KNC-BGO	this work	STDPipe
2022-10-10T03:01:14	59862.1262	0.5727	i'	300s	16.44 ± 0.06	17.8 (5σ)	KNC-BGO	this work	STDPipe
2022-10-10T03:06:48	59862.1301	0.5766	i'	300s	16.58 ± 0.07	17.8 (5σ)	KNC-BGO	this work	STDPipe
2022-10-10T04:26	59862.1847	0.6313	i'	60×5s	16.41 ± 0.05	19.56	LOAO-1m	Paek et al. (2022)	-
2022-10-10T12:25	59862.5174	0.9639	i'	2×150s	17.38 ± 0.09	-	SLT-40	Chen et al. (2022)	-
2022-10-10T16:59	59862.716	1.1625	i'	9×80s	17.67 ± 0.05	20.7	KAO	this work	Muphoten
2022-10-10T17:23	59862.7243	1.1708	i'	15×30s	17.58 ± 0.01	20.7 (3σ)	AZT-20	Belkin et al. (2022a)	-
2022-10-10T17:17	59862.7201	1.1667	i'	600s	17.52 ± 0.01	-	RTT-150	Bikmaev et al. (2022a)	-
2022-10-10T18:20:07	59862.7938	1.2255	i'	14×180s	17.47 ± 0.09	17.6 (5σ)	KNC-IRIS	this work	STDPipe
2022-10-10T19:26	59862.8097	1.2563	i'	2×300s	17.5 ± 0.12	-	RC-80	Vinko et al. (2022)	-
2022-10-10T21:01	59862.8757	1.3222	i'	600s	17.69 ± 0.02	-	RTT-150	Bikmaev et al. (2022a)	-
2022-10-11T06:07:28	59863.2569	1.7035	i'	300s	17.85 ± 0.13	18.1 (5σ)	KNC-iT24	this work	STDPipe
2022-10-11T06:12:57	59863.2607	1.7072	i'	300s	18.24 ± 0.22	18.2 (5σ)	KNC-iT24	this work	STDPipe
2022-10-11T00:54	59863.0375	1.484	i'	-	17.92 ± 0.06	-	BlackGEM	Groot et al. (2022)	-
2022-10-11T16:48	59863.7	2.1465	i'	600s	18.4 ± 0.02	-	RTT-150	Bikmaev et al. (2022a)	-
2022-10-11T18:46:47	59863.8193	2.2659	i'	199×32s	18.64 ± 0.21	18.7 (5σ)	KNC-EHEA-200F5	this work	STDPipe
2022-10-11T20:56	59863.8722	2.3188	i'	600s	18.49 ± 0.04	-	RTT-150	Bikmaev et al. (2022a)	-
2022-10-12T00:58:02	59864.0626	2.5092	i'	11 × 300s	18.44 ± 0.09	19.0 (5σ)	KNC-BGO	this work	STDPipe
2022-10-12T02:07:18	59864.1083	2.5548	i'	11×300s	18.74 ± 0.13	19.3 (5σ)	KNC-C11-FREE	this work	STDPipe
2022-10-12T02:40	59864.1111	2.5577	i'	-	19.0 ± 0.2	-	LBTO	Shresta et al. (2022)	-
2022-10-12T03:34	59864.1486	2.5952	i'	3×300s	-	20.5	LCOGT	Strausbaugh (2022b)	-
2022-10-12T16:54	59864.7042	3.1507	i'	600s	18.82 ± 0.03	-	RTT-150	Bikmaev et al. (2022a)	-
2022-10-12T17:27	59864.7271	3.1736	i'	600s	19.02 ± 0.07	-	RTT-150	Bikmaev et al. (2022a)	-
2022-10-12T17:59	59864.7493	3.1958	i'	600s	19.09 ± 0.1	-	RTT-150	Bikmaev et al. (2022a)	-
2022-10-12T18:31	59864.7715	3.2181	i'	600s	18.95 ± 0.07	-	RTT-150	Bikmaev et al. (2022a)	-
2022-10-12T19:03	59864.7938	3.2403	i'	600s	18.93 ± 0.04	-	RTT-150	Bikmaev et al. (2022a)	-
2022-10-12T19:36	59864.8167	3.2632	i'	600s	18.93 ± 0.04	-	RTT-150	Bikmaev et al. (2022a)	-
2022-10-12T19:40	59864.8194	3.266	i'	3×600s	18.91 ± 0.11	-	OHP	Schneider et al. (2022)	-
2022-10-12T20:08	59864.8389	3.2854	i'	600s	18.92 ± 0.04	-	RTT-150	Bikmaev et al. (2022a)	-
2022-10-12T20:18	59864.8458	3.2924	i'	300s	18.74 ± 0.18	-	RC-80	Vinko et al. (2022)	-

Table 4. Continued.

2022-10-13T02:36:45	59865.1069	3.5534	i'	12 × 300s	19.50 ± 0.22	19.4 (5σ)	KNC-BGO	this work	STDPIPE
2022-10-13T02:24:22	59865.1149	3.5614	i'	20×120s	-	18.7 (5σ)	KNC-iT11	this work	STDPIPE
2022-10-13T03:09	59865.1312	3.5778	i'	-	19.37 ± 0.05	-	LDT	O'Connor et al. (2022a)	-
2022-10-13T17:04	59865.7111	4.1577	i'	600s	19.51 ± 0.06	-	RTT-150	Bikmaev et al. (2022b)	-
2022-10-13T17:36	59865.7333	4.1799	i'	600s	19.41 ± 0.05	-	RTT-150	Bikmaev et al. (2022b)	-
2022-10-13T18:09	59865.7562	4.2028	i'	600s	19.52 ± 0.05	-	RTT-150	Bikmaev et al. (2022b)	-
2022-10-13T17:42	59865.7642	4.2108	i'	21×110s	19.73 ± 0.3	20.3	KAO	this work	MUPHOTEN
2022-10-13T18:41	59865.7785	4.225	i'	600s	19.44 ± 0.04	-	RTT-150	Bikmaev et al. (2022b)	-
2022-10-13T19:13	59865.8007	4.2472	i'	600s	19.45 ± 0.05	-	RTT-150	Bikmaev et al. (2022b)	-
2022-10-13T19:46	59865.8236	4.2702	i'	600s	19.43 ± 0.05	-	RTT-150	Bikmaev et al. (2022b)	-
2022-10-13T20:18	59865.8458	4.2924	i'	600s	19.48 ± 0.06	-	RTT-150	Bikmaev et al. (2022b)	-
2022-10-13T20:53	59865.8701	4.3167	i'	600s	19.5 ± 0.07	-	RTT-150	Bikmaev et al. (2022b)	-
2022-10-14T00:04	59866.0028	4.4493	i'	-	19.89 ± 0.05	-	VLT	Izzo et al. (2022)	-
2022-10-14T00:40	59866.0278	4.4743	i'	7×60s	19.8 ± 0.5	-	GMOS	Rastinejad & Fong (2022)	-
2022-10-15T06:34	59867.2736	5.7202	i'	-	20.01 ± 0.05	-	Faulkes	Shrestha et al. (2022)	-
2022-10-15T14:11	59867.591	6.0375	i'	30×60s	20.0 ± 0.04	23.2 (3σ)	AZT-20	Belkin et al. (2022a)	-
2022-10-19T02:05	59871.0868	9.5333	i'	-	20.72 ± 0.05	-	LDT	O'Connor et al. (2022b)	-
2022-10-21T15:04	59873.6278	12.0743	i'	30×60s	20.72 ± 0.11	23.3(3σ)	AZT-20	Belkin et al. (2022b)	-
2022-10-29T06:09	59881.2632	19.7097	i'	2×300s	21.87 ± 0.05	24.5	CFHT-Megacam	this work	STDPIPE & MUPHOTEN
2022-10-09T20:05:19	59861.8422	0.2887	I_c	5×180s	15.21 ± 0.04	17.0 (5σ)	KNC-SCT-0.28	this work	MUPHOTEN
2022-10-10T05:00	59862.2083	0.6549	I_c	300s	16.74 ± 0.1	-	Nickel-1m	Vidal et al. (2022)	-
2022-10-10T11:39	59862.4854	0.932	I_c	8340s	17.1 ± 0.2	-	MITSuME	Sasada et al. (2022)	-
2022-10-10T20:04:25	59862.8436	1.2902	I_c	7×180s	17.12 ± 0.13	17.0 (5σ)	KNC-SCT-0.28	this work	MUPHOTEN
2022-10-11T18:14	59863.7958	2.2424	I_c	52×60s	-	-	AbAO-T70	this work	VETO
2022-10-11T21:06:16	59863.9043	2.3509	I_c	24×180s	-	17.6 (5σ)	KNC-SCT-0.28	this work	MUPHOTEN
2022-10-12T18:11	59864.7889	3.2354	I_c	45×60s	-	-	Lisnyky-AZT-8	this work	VETO
2022-10-13T01:49:56	59865.1248	3.5713	I_c	23×300s	18.95 ± 0.12	19.7 (5σ)	KNC-C11-FREE	this work	STDPIPE
2022-10-15T18:44	59867.8639	6.3104	I_c	120×60s	19.77 ± 0.17	19.0	Lisnyky-AZT-8	this work	MUPHOTEN
2022-10-24T23:01	59877.0383	15.4848	I_c	685×10s	-	19.8	VIRT	this work	MUPHOTEN
2022-10-09T18:29	59861.7701	0.2167	z'	6×60s	14.89 ± 0.03	-	MeerLICHT	de Wet et al. (2022)	-
2022-10-10T12:25	59862.5174	0.9639	z'	2×150s	16.6 ± 0.09	-	SLT-40	Chen et al. (2022)	-
2022-10-10T17:26	59862.7264	1.1729	z'	15×30s	16.87 ± 0.05	19.8	AZT-20	Belkin et al. (2022a)	-
2022-10-10T17:28	59862.7278	1.1743	z'	600s	16.81 ± 0.01	-	RTT-150	Bikmaev et al. (2022a)	-
2022-10-10T17:15	59862.728	1.1745	z'	10×80s	16.97 ± 0.06	20.3	KAO	this work	MUPHOTEN
2022-10-10T21:13	59862.884	1.3306	z'	600s	16.99 ± 0.01	-	RTT-150	Bikmaev et al. (2022a)	-
2022-10-11T00:50	59863.0347	1.4813	z'	-	16.92 ± 0.05	-	BlackGEM	Groot et al. (2022)	-
2022-10-11T16:59	59863.7076	2.1542	z'	600s	17.69 ± 0.02	-	RTT-150	Bikmaev et al. (2022a)	-
2022-10-11T21:07	59863.8799	2.3264	z'	600s	17.72 ± 0.03	-	RTT-150	Bikmaev et al. (2022a)	-
2022-10-12T02:40	59864.1111	2.5577	z'	-	18.26 ± 0.01	-	LBTO	Shresta et al. (2022)	-
2022-10-12T14:34	59864.6092	3.0557	z'	-	18.40 ± 0.11	-	GMG-Lijiang	(Mao et al. 2022)	-
2022-10-12T17:16	59864.7194	3.166	z'	600s	18.2 ± 0.04	-	RTT-150	Bikmaev et al. (2022a)	-
2022-10-12T17:48	59864.7417	3.1882	z'	600s	18.19 ± 0.05	-	RTT-150	Bikmaev et al. (2022a)	-
2022-10-12T18:21	59864.7646	3.2111	z'	600s	18.4 ± 0.08	-	RTT-150	Bikmaev et al. (2022a)	-
2022-10-12T18:53	59864.7868	3.2333	z'	600s	18.26 ± 0.03	-	RTT-150	Bikmaev et al. (2022a)	-
2022-10-12T19:25	59864.809	3.2556	z'	600s	18.23 ± 0.03	-	RTT-150	Bikmaev et al. (2022a)	-
2022-10-12T19:40	59864.8194	3.266	z'	2100s	18.35 ± 0.13	-	OHP	Schneider et al. (2022)	STDPIPE
2022-10-12T19:57	59864.8312	3.2778	z'	600s	18.23 ± 0.04	-	RTT-150	Bikmaev et al. (2022a)	-
2022-10-12T20:35	59864.8576	3.3042	z'	600s	18.3 ± 0.04	-	RTT-150	Bikmaev et al. (2022b)	-
2022-10-12T21:08	59864.8806	3.3271	z'	600s	18.18 ± 0.04	-	RTT-150	Bikmaev et al. (2022b)	-
2022-10-13T17:15	59865.7188	4.1653	z'	600s	18.63 ± 0.05	-	RTT-150	Bikmaev et al. (2022b)	-
2022-10-13T17:47	59865.741	4.1875	z'	600s	18.76 ± 0.05	-	RTT-150	Bikmaev et al. (2022b)	-
2022-10-13T18:19	59865.7632	4.2097	z'	600s	18.69 ± 0.04	-	RTT-150	Bikmaev et al. (2022b)	-
2022-10-13T17:51	59865.7705	4.217	z'	21×110s	18.90 ± 0.16	19.8	KAO	this work	MUPHOTEN
2022-10-13T18:52	59865.7861	4.2327	z'	600s	18.75 ± 0.04	-	RTT-150	Bikmaev et al. (2022b)	-
2022-10-13T19:24	59865.8083	4.2549	z'	600s	18.74 ± 0.05	-	RTT-150	Bikmaev et al. (2022b)	-
2022-10-13T19:57	59865.8312	4.2778	z'	600s	18.83 ± 0.05	-	RTT-150	Bikmaev et al. (2022b)	-
2022-10-13T20:32	59865.8556	4.3021	z'	600s	18.74 ± 0.05	-	RTT-150	Bikmaev et al. (2022b)	-
2022-10-13T21:06	59865.8792	4.3257	z'	600s	18.71 ± 0.06	-	RTT-150	Bikmaev et al. (2022b)	-
2022-10-14T12:12	59866.5106	4.9571	z'	-	19.21 ± 0.12	-	GMG-Lijiang	(Mao et al. 2022)	-
2022-10-15T06:34	59867.2736	5.7202	z'	-	19.39 ± 0.05	-	Faulkes	Shrestha et al. (2022)	-
2022-10-15T16:08	59867.6722	6.1188	z'	15×60s	19.31 ± 0.08	21.0 (3σ)	AZT-20	Belkin et al. (2022a)	-
2022-10-22T16:22	59874.7375	13.184	z'	20×240s	-	20.4	KAO	this work	MUPHOTEN
2022-10-29T06:32	59881.2843	19.7308	z'	4×260s	21.01 ± 0.08	24.0	CFHT-Megacam	this work	MUPHOTEN
2022-10-09T15:30	59861.6458	0.0924	Clear	180s	15.5 ± 0.1	-	SCT	Odeh (2022)	-
2022-10-09T15:49	59861.659	0.1056	Clear	180s	15.6 ± 0.1	-	SCT	Odeh (2022)	-
2022-10-09T17:14	59861.7181	0.1646	Clear	180s	15.9 ± 0.1	-	SCT	Odeh (2022)	-
2022-10-09T18:44	59861.7806	0.2271	Clear	×60s	16.21 ± 0.11	-	BOOTES-2	Hu et al. (2022)	-
2022-10-10T19:29	59862.8257	1.2722	Clear	20×60s	18.52 ± 0.06	19.5	MOSS	this work	MUPHOTEN
2022-10-10T19:31	59862.8490	1.2955	L	34×180s	18.38 ± 0.25	20.2 (3σ)	KNC-HAO	this work	MUPHOTEN
2022-10-10T21:48:00	59862.9188	1.3652	CR	10×180s	18.76 ± 0.14	19.2 (5σ)	KNC-MSXD	this work	STDPIPE
2022-10-11T16:33	59863.7069	2.1535	Clear	10×150s	-	17.5	SNOVA	this work	MUPHOTEN
2022-10-11T18:29:21	59863.7707	2.2172	CR	2×30s	-	18.3 (5σ)	KNC-Montarrenti	this work	STDPIPE
2022-10-11T18:24:14	59863.7825	2.2290	CR	15×180s	19.22 ± 0.08	20.3	KNC-MSXD	this work	STDPIPE
2022-10-11T18:27:11	59863.8203	2.2668	L	3×2960s	-	19.7 (5σ)	KNC-COK26	this work	STDPIPE
2022-10-12T13:56	59864.5979	3.0445	Clear	10×150s	-	19.1	SNOVA	this work	MUPHOTEN
2022-10-14T18:17:29	59866.7944	5.2409	CR	31×180s	20.63 ± 0.11	21.3 (5σ)	KNC-MSXD	this work	STDPIPE
2022-10-14T20:13:33	59866.8768	5.3233	CR	180×32s	20.46 ± 0.14	21.0 (5σ)	KNC-T-CAT	this work	STDPIPE
2022-10-15T19:17:26	59867.8329	6.2795	CR	28×180s	20.75 ± 0.13	21.3 (5σ)	KNC-MSXD	this work	STDPIPE